Published November 15, 2018

Special Section: Hydrological Observatories

Core Ideas

- Studying the critical zone requires targeted research on water, energy, gas, solutes, and sediments.
- The SSHCZO targets a 165-km^2 watershed on sedimentary rocks in the northeastern United States.
- One SSHCZO subcatchment, Shale Hills, provides extraordinary data describing a shale CZ.

Susquehanna Shale Hills Critical Zone Observatory: Shale Hills in the Context of Shaver's Creek Watershed

Susan L. Brantley,* Tim White, Nicole West, Jennifer Z. Williams, Brandon Forsythe, Dan Shapich, Jason Kaye, Henry Lin, Yuning Shi, Margot Kaye, Elizabeth Herndon, Kenneth J. Davis, Yuting He, David Eissenstat, Julie Weitzman, Roman DiBiase, Li Li, Warren Reed, Kristen Brubaker, and Xin Gu

The Susquehanna Shale Hills Critical Zone Observatory (SSHCZO) was established to investigate the form, function, and dynamics of the critical zone developed on sedimentary rocks in the Appalachian Mountains in central Pennsylvania. When first established, the SSHCZO encompassed only the Shale Hills catchment, a 0.08-km^2 subcatchment within Shaver's Creek watershed. The SSHCZO has now grown to include 120 km^2 of the Shaver's Creek watershed. With that growth, the science team designed a strategy to measure a parsimonious set of data to characterize the critical zone in such a large watershed. This parsimonious design includes three targeted subcatchments (including the original Shale Hills), observations along the main stem of Shaver's Creek, and broad topographic and geophysical observations. Here we describe the goals, the implementation of measurements, and the major findings of the SSHCZO by emphasizing measurements of the main stem of Shaver's Creek as well as the original Shale Hills subcatchment.

Abbreviations: ANPP, aboveground net primary productivity; CZ, critical zone; CZO, critical zone observatory; ET, evapotranspiration; NEP, net ecosystem productivity; SSHCZO, Susquehanna Shale Hills Critical Zone Observatory.

S.L. Brantley, T. White, J.Z. Williams, B. Forsythe, D. Shapich, K.J. Davis, and R. DiBiase, Earth and Environmental Systems Institute, Pennsylvania State Univ., University Park, PA 16802; N. West, Dep. of Earth and Atmospheric Sciences, Central Michigan Univ., Mt. Pleasant, MI 48859; J. Kaye, H. Lin, and Y. Shi, Dep. of Ecosystem Science and Management, Pennsylvania State Univ., University Park, PA 16802; M. Kaye, D. Eissenstat, and W. Reed, Dep. of Ecosystem Science and Management and Intercollege Graduate Degree Program in Ecology, Pennsylvania State Univ., University Park, PA 16802; E. Herndon, Dep. of Geology, Kent State Univ., Kent, OH 44240; K.J. Davis and Y. He, Dep. of Meteorology and Atmospheric Science, Pennsylvania State Univ., University Park, PA 16802; J. Weitzman, CUNY Advanced Science Research Center, New York, NY 10031; J. Weitzman, Cary Institute of Ecosystem Studies, Millbrook, NY 12545; L. Li, Dep. of Civil and Environmental Engineering, Pennsylvania State Univ., University Park, PA 16802; K. Brubaker, Environmental Studies, Hobart and William Smith Colleges, Geneva, NY 14456; X. Gu, Dep. of Geosciences, Pennsylvania State Univ., University Park, PA 16802. *Corresponding author (brantley@eesi.psu.edu).

Received 30 Apr. 2018.
Accepted 5 Aug. 2018.
Supplemental material online.

Citation: Brantley, S.L., T. White, N. West, J.Z. Williams, B. Forsythe, D. Shapich, J. Kaye, H. Lin, Y. Shi, M. Kaye, E. Herndon, K.J. Davis, Y. He, D. Eissenstat, J. Weitzman, R. DiBiase, L. Li, W. Reed, K. Brubaker, and X. Gu. 2018. Susquehanna Shale Hills Critical Zone Observatory: Shale Hills in the context of Shaver's Creek watershed. Vadose Zone J. 17:180092. doi:10.2136/vzj2018.04.0092

© Soil Science Society of America.
This is an open access article distributed under the CC BY-NC-ND license (http://creativecommons.org/licenses/by-nc-nd/4.0/).

Critical zone observatories (CZOs) have nucleated around the world to investigate the entire zone from the top of vegetation canopy to groundwater (Brantley et al., 2017b). As one of the first three CZOs in the United States, the Susquehanna Shale Hills CZO (SSHCZO) originally focused on a small watershed underlain almost entirely by shale (Shale Hills). In 2013, the footprint of the CZO increased from just Shale Hills (Lin, 2006; Qu and Duffy, 2007; Lin and Zhou, 2008) to 120 km^2 of the 165-km^2 Shaver's Creek watershed (Fig. 1). The goal of all CZOs is to answer three questions: What controls the critical zone (CZ) properties and processes? How will critical zone structure, stores, and fluxes respond to climate and land use change? How can improved understanding of the critical zone be used to enhance CZ services? Critical zone services are like the more common concept of ecosystem services except that they are extended to the entire CZ (Field et al., 2015).

Each CZO also has its own focus. The focus of the SSHCZO in its expanded form is to learn to project CZ form and function into the near future—i.e., "earthcast"—and to learn how to upscale our understanding from small footprints like Shale Hills to larger, more regional footprints such as the Shaver's Creek watershed. The larger watershed encompasses not only more lithologies, but also includes relatively pristine landscapes that are forested but where land use includes agriculture, managed forests, and minor development. From 2013 to 2017 we have been grappling with how to expand from our earlier paradigm at Shale Hills, where the small size allowed us to "measure everything, everywhere," to a more realistic paradigm in Shaver's Creek of "measuring only what is needed." In short, our larger 120-km^2 footprint has necessitated an extremely parsimonious

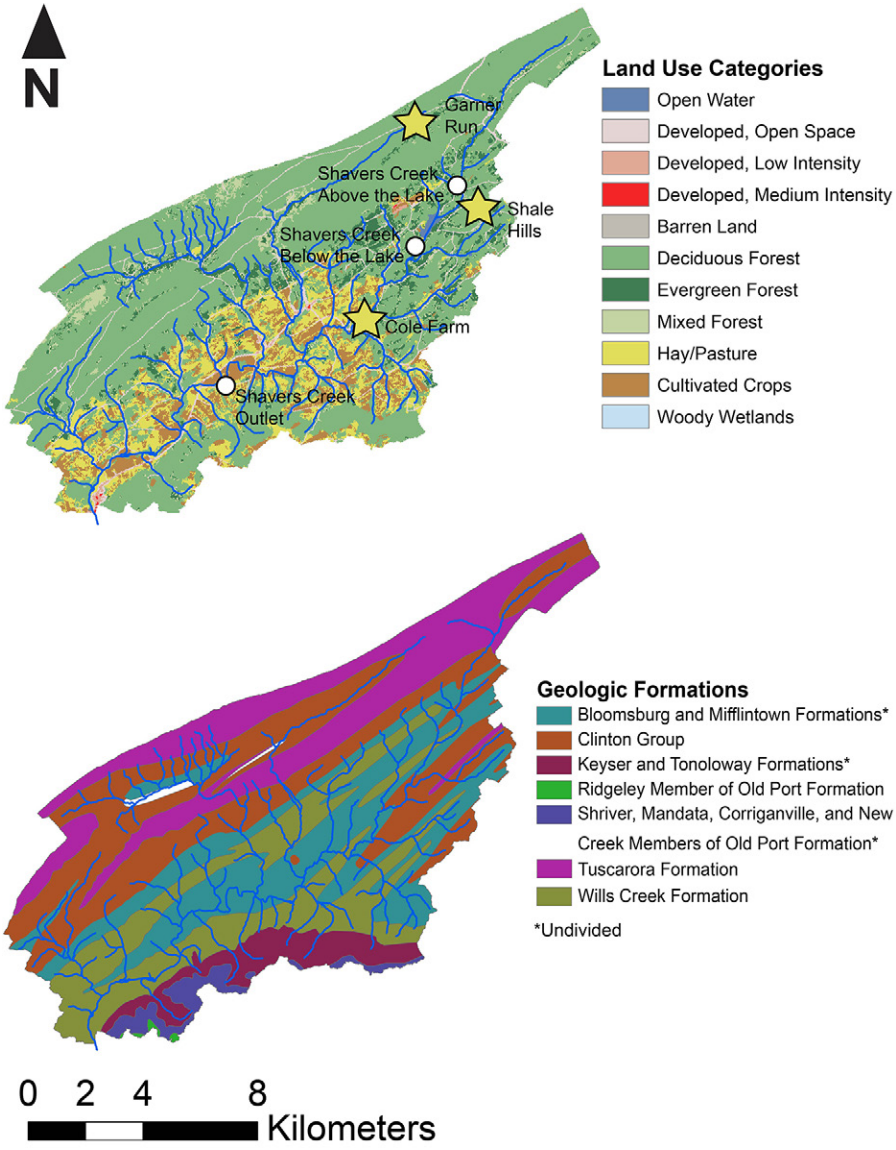

Fig. 1. Land use map for Shaver's Creek watershed (165 km^2), showing the three nested subcatchments (stars) and some of the monitoring sites on Shaver's Creek main stem (upper), and geological map of the watershed (bottom). The Susquehanna Shale Hills Critical Zone Observatory includes 120 km^2 of the upper Shaver's Creek watershed, i.e., above the point labeled Shaver's Creek Outlet.

implementation of instruments and measurements as we learn to upscale and earthcast the future (Brantley et al., 2016).

To upscale the CZO, we (i) continue to investigate the original Shale Hills subcatchment; (ii) are now monitoring two small subcatchments in addition to Shale Hills; (iii) are also monitoring several sites along the main stem of Shaver's Creek for chemistry and discharge (Fig. 1); and (iv) are using topographic and geophysical measurements to link together observations (Brantley et al., 2016). Here, we focus on measurements of the main stem and in the Shale Hills subcatchment. Li et al. (2018) summarizes the two new subcatchments (Garner Run and Cole Farm). The hypothesis underlying our choice of three subcatchments is that characteristics that differ in the subcatchments are pivotal in affecting CZ function (Table 1). By measuring and modeling the subcatchments separately, we can learn to upscale to the entire watershed using topographic data, geophysical measurements, models, and main-stem chemistry and discharge data.

Table 1. Key geomorphological characteristics among the subcatchments.

Site	Drainage density	Slope	Land use	Soil
Shale Hills	high	moderate	forested	fine-grained
Cole Farm	medium	low	farmed	fine-grained
Garner Run	very low	moderate	forested	coarse-grained

Motivation and Science Questions

The upscaling from Shale Hills has forced us to grapple with how to transition from measuring "everything, everywhere" to measuring "only what is needed" and to understand how to deal with the effects of multiple lithologies and land use characteristics (Brantley et al., 2016). For example, to limit the number of soil pit measurements, we have designed an implementation, referred to as GroundHOG (Hydrological Observation Gear), that was described previously (Brantley et al., 2016). While the topic of upscaling has long been tackled in the hydrologic literature (Sposito, 1998; Li et al., 2017b; Wen and Li, 2018), the topic of upscaling models of the entire CZ has not been well investigated. We are

using models as well as publicly available satellite, topography, geophysical, and map data (e.g., soils and land use) to extrapolate from spot measurements of soils and fluxes to the broader watershed. We are testing the following overarching hypothesis: To project CZ evolution into the future requires knowledge of geological history, observations of CZ processes today, and scenarios of human activities tomorrow. Such projections—which we refer to as earthcasts—require scenarios of changing climate and land use into the future (e.g., Godderis and Brantley, 2014).

Subcatchment Characteristics

Geological Structure and Climate

Structure

The Shale Hills subcatchment is a small (0.08 km^2), first-order watershed entirely underlain by the Silurian-aged Clinton Group consisting primarily of the Fe-rich, organic-poor shale of the Rose Hill Formation (Swain, 1966, p. 1–21; Meyer et al., 1992) and to a much lesser extent by the stratigraphically younger Keefer Sandstone (Sullivan et al., 2016a). Overall, the Rose Hill Formation coarsens upward, and the upper third consists of interbedded sandstone, limestone, and shale (Cotter and Inners, 1986). Linear features observable in high-resolution lidar-derived topography mark the contact between the Rose Hill Formation and Keefer Sandstone along the mouth of the Shale Hills watershed and adjacent subcatchments (Fig. 2).

The catchment is located on the northwest-dipping limb of a third-order anticline in the Broadtop Synclinorium, the westernmost of the synclinoria in the Ridge and Valley physiographic province. The third-order anticline plunges to the southwest, with bedding strike at approximately N54E. Dip angles calculated from the geologic map range from 19 to 26° depending on what formation thickness is applied, but these dips are dissimilar to those measured in the field in and around the catchment. This disparity probably reflects more complex, smaller scale structures such as small folds within the catchment.

Given the limited outcrops and difficulty in identifying bedding in the very fissile and fractured shale, dip was measured in exposures in and near to the catchment, in soil pits, borehole logs (Sullivan et al., 2016a), and in petrographic thin sections from oriented samples. These dip measurements (48–88° through the shale-underlain part of the catchment) are ~20° to 60° steeper than the dips indicated by the existing geologic maps. Dips vary between northwesterly and southeasterly within the catchment (see Fig. 3A), consistent with inclined tight asymmetric fourth (or more)-order folds. At Greenwood Furnace State Park ~12 km to the southeast, the Rose Hill Formation is well exposed in a similar structural position and displays tight, meter- to decimeter-scale folds through the shale-dominated portions of the formation (see Fig. 3B).

The shallowest dips are measured in pits and borehole logs in the mouth of the catchment near the outcropping Keefer Sandstone. This observation is consistent with observations made in nearby Barree, PA, where the Rose Hill Formation–Keefer Sandstone contact is well exposed and shows gently dipping strata on the upper limb of a northwest-vergent higher order anticline (see Fig. 3C).

Geomorphological and Climate Observations

Shale Hills is bound by low ridges to the north and south (relief ~ 30 m), with an ephemeral, westward-flowing stream that

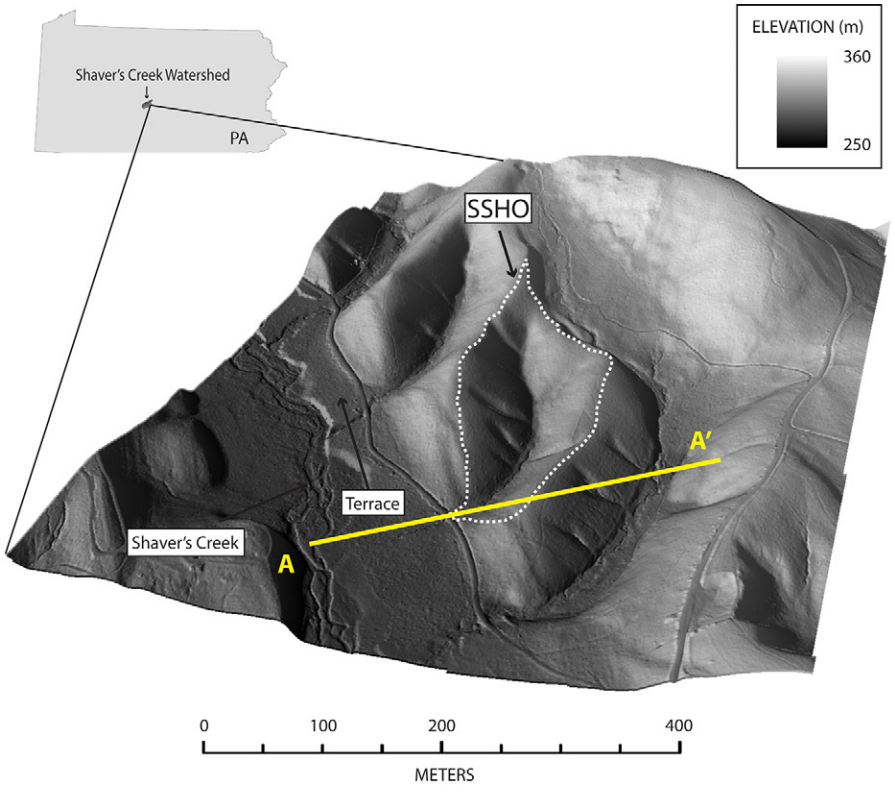

Fig. 2. Shaded relief perspective image of the Shale Hills watershed (labeled SSHO) overlain on a digital elevation model. All layers created from high-resolution lidar-derived digital elevation data collected in cooperation with the National Center for Airborne Laser Mapping (opentopography.com; Guo, 2010). Imaging reveals a braided stream draining to the main stem Shaver's Creek. The SSHO catchment exhibits low relief and contains a subtle fill terrace into which the present day channel incises. Figure reproduced with permission from West et al. (2013).

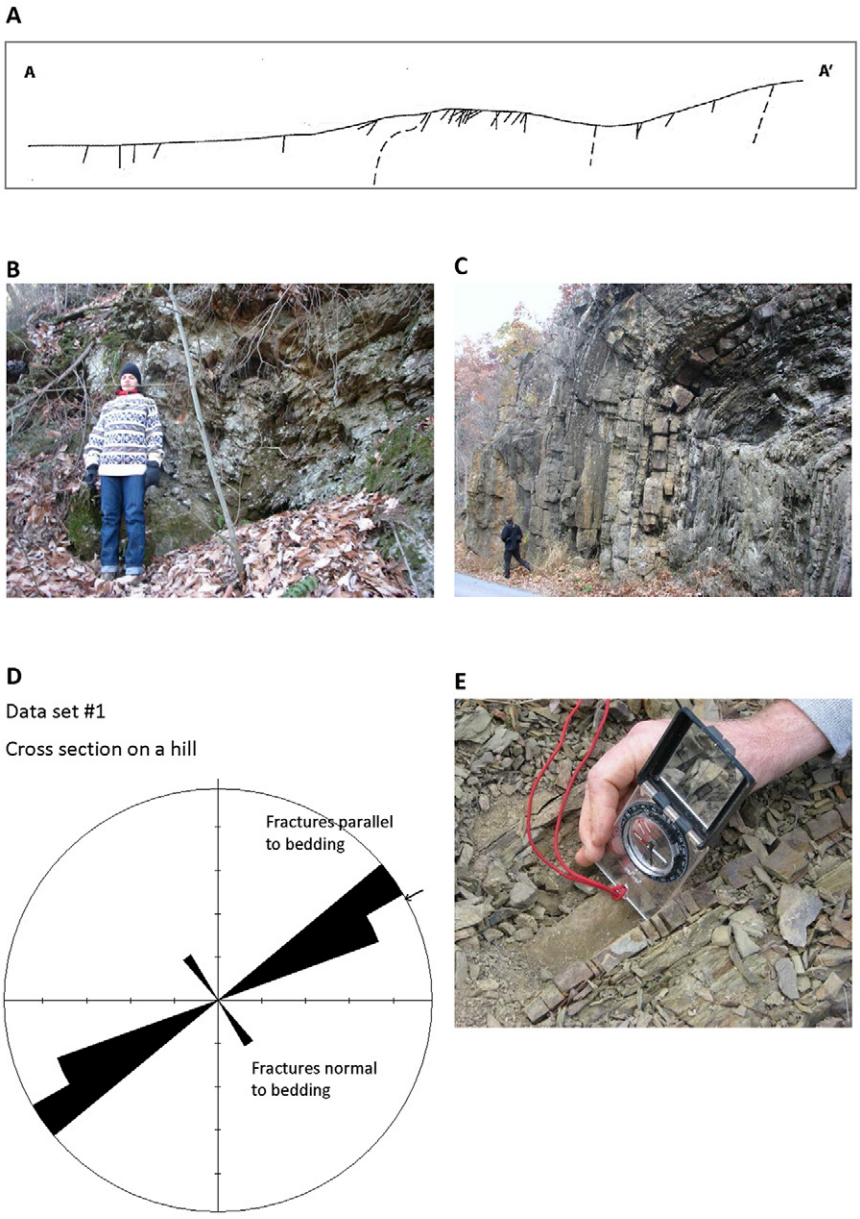

Fig. 3. (A) Cross-section drafted perpendicular to strike showing topographic profile along line A–A′ (see Fig. 2 for location), with dips from outcrops and soil pits extrapolated laterally to the line of section. The dips show tight asymmetric folds like those observed regionally (see B). Note that dashed lines represent dips inferred from subsurface well observations and also that the folded dashed line to the left in the diagram is based on well observations of the Keefer Sandstone and is similar to the image shown in C. (B) A tight asymmetric fold in the Rose Hill Formation at Greenwood Furnace State Park. (C) The northwest-vergent anticline at Barree, PA. (D) Rose diagram of fracture orientations measured from soil pits dug to bedrock and outcrops surrounding the Shale Hills subcatchment. Dominant average strike is N50E. The arrow marks the average strike of N54E. Most fractures in the Rose Hill Formation are parallel or slightly oblique to bedding, whereas a small subset are oriented normal to bedding (see E). (E) Outcrop photograph showing relatively thicker and more massive fine sandstone interbeds (at compass) with widely spaced fractures normal to bedding and laminated mudstone to shale exhibiting numerous fractures parallel and slightly oblique to bedding at quarry site north of Shale Hills.

flows into Shaver's Creek and eventually joins the Juniata and eventually the Susquehanna River. Ridgelines are approximately perpendicular to the bedding strike at the mouth of the Shale Hills catchment watershed, but become more oblique toward the head of the catchment.

Hillslopes at Shale Hills are generally convex upward and planar, with few regions of convergent topography (swales). Hillslopes also become concave upward toward the channel. Hillslopes along the south side of the watershed are consistently steeper than on the north slopes by 5 to 10°. Along the most planar hillslopes, soils are thin near the ridges (~30 cm) and thicken downslope. Along planar regions of the north slopes, soils are consistently thin (~50 cm) and immediately overlie fractured bedrock (West et al., 2013, 2014). On the south slopes, soil thickness is more variable and generally thicker (~80 cm), overlying an ~2-m-thick layer of coarse, open-framework talus that extends across the slope from the midslope position to the valley floor, where it interfingers with alluvial fill (West et al., 2013, 2014). All of these features are consistent with higher energy sediment transport conditions in recent geological history than observed today.

This change in transport conditions is probably related to the Shale Hills location. Lying 75 km south of the Laurentide Ice Margin, Shale Hills experienced a periglacial climate as recently as 15,000 yr ago (Braun, 1989). Evidence of this periglacial history is found throughout the region as solifluction lobes on high quartzite ridges, ice wedges, and greze letees (Clark and Ciolkosz, 1988; Ciolkosz et al., 1989). Evidence of a periglacial climate is more subtle within the Shale Hills watershed but can be discerned in the record of changing sediment loads (West et al., 2013). The stream within Shale Hills incises into alluvial fill that is approximately 2.5 m deep along the valley floor (West et al., 2013), consistent with previous aggradation events. Similarly, lidar-derived digital topography reveals that Shaver's Creek flows along a remnant braided channel bounded by a subtle terrace formed just downstream of Shale Hills.

Today, the mean annual temperature is 10°C and mean annual precipitation is 1070 mm (NOAA, 2007). Derived quantities for the catchment are summarized in Table 2 with respect to erosion and weathering.

Character of Rock and Soil in Shale Hills

The Rose Hill Formation shale is characterized by fracture sets of three orientations: (i) bedding parallel, (ii) slightly oblique to bedding, and (iii) normal to bedding (see Fig. 3D and 3E). Rose Hill shale is olive-pink to grayish buff and is generally not as fractured below the water table as above. Jin et al. (2011a) referred to this relatively unfractured and unweathered rock as *bedrock*, and referred to all the fractured and somewhat weathered rock material above bedrock that could not be hand-augered as *saprock*. In addition, the upper 5 to 8 m of this saprock throughout the catchment (directly under the augerable soil) is more highly fractured than below, as shown in Fig. 2 (Jin et al., 2010, 2011b; Kuntz et al., 2011; Slim et al., 2015).

Bedrock composition varies but includes illite, quartz, chlorite, feldspar, Ti and Fe oxides, and minor apatite, zircon, and monazite. Deep weathering fronts have been identified in the watershed: both ankerite and pyrite dissolve at depths either near or beneath today's water table and are largely absent above; chlorite begins to oxidize and lose Mg at or above the water table to increasingly form vermiculitized chlorite and hydroxy-interlayered vermiculite at shallower depths; feldspar begins to dissolve at the base of the upper fractured zone; and illite begins to weather in the augerable soil—these latter two reactions produce minor kaolinite observed in the soil (Jin et al., 2010, 2011a; Brantley et al., 2013; Brantley et al., 2017a). More than 90% of the water that enters the catchment infiltrates the soil and fractured upper saprock and flows down to the valley along preferential flow lines through the upper soil and upper fractured layers (Guo et al., 2014; Zhang et al., 2014; Sullivan et al., 2016a). The rest of the water infiltrates down to the deeper oxidized zone and exits the watershed as deep groundwater flow (Fig. 4). Residence times of water in the catchment have been estimated based on water isotopes and other tracers and are always less than a few decades (Thomas et al., 2013; Sullivan et al., 2016b).

Table 2. Relief, erosion, and weathering estimates for Shale Hills catchment.

Parameter	Estimate
Ridge–valley relief	
Surface relief	22 ± 8 m, ~24 m (ridge vs. channel)
Bedrock relief	~4 m (unweathered bedrock under ridge vs. channel)
Porosity of bedrock	5% (Jin et al., 2011b)
Saturated bedrock hydraulic conductivity	2.7×10^{-15} m s^{-1} (Kuntz et al., 2011)
Weathered bedrock bulk density	2.60 g cm^{-3} (Jin et al., 2010)
Soil bulk density (including all rock fragments)	1.8 g cm^{-3} (Jin et al., 2010)
Estimated slope of the regional water table	~4%
Mean estimated slope of surface topography	
North facing	27 ± 4%
South facing	36 ± 7%
Soil diffusivity	27 to 187 cm^2 yr^{-1} (West, 2014)
Hillslope length	80 ± 30 m at the channel
Catchment erosion rate	15 m Myr^{-1} (Jin et al., 2010)
Soil erosion rate	16–19 m Myr^{-1} (West et al., 2013)
Soil production rate	39–45 m Myr^{-1} (Ma et al., 2010, 2013)

The thickness of the augerable soil (depth to the top of saprock) was measured catchment-wide using auger sampling (318 auger points) and contoured using regression kriging (Isaaks and Srivastava, 1989; Odeh et al., 1995) and a backward-stepwise algorithm. The soils, formed from both residuum and colluvium, are generally classified as silt loams and silty clay loams with respect to texture, with some clay loams and sandy clay loams. All soil types have an approximately 0.05-m-thick litter layer (Oe horizon). Many gravelly shale fragments (2–150 mm) are found throughout the soil profiles. Fragment size generally decreases upward in the soils (Brantley et al., 2011). The soils at Shale Hills have also been compared with soils along a climosequence also developed on Rose Hill shale or other geochemically similar shales (Dere et al., 2013).

A detailed soil survey, conducted in cooperation with the USDA–NRCS (Lin, 2006), analyzed 289 samples. Soil series (Weikert [loamy-skeletal, mixed, active, mesic Lithic Dystrudepts], Rushtown [loamy-skeletal over fragmental, mixed, active, mesic Typic Dystrudepts], Berks [loamy-skeletal, mixed, active, mesic Typic Dystrudepts], Blairton [fine-loamy, mixed, active, mesic Aquic Hapludults], and Ernest [fine-loamy, mixed, superactive, mesic Aquic Fragiudults]) were identified in the catchment based on thickness, landscape position, and depth to redoximorphic features. Soil organic carbon has also been measured in the catchment (Andrews, 2011; Andrews et al., 2011).

Vegetation in Shale Hills

The Shale Hills subcatchment is covered by a mature forest dominated by oak species (64% of the basal wood area and 75% of the annual wood growth) and includes a diverse community of 23 canopy tree species. Overall, aboveground net primary productivity is 443 g C m^{-2} yr^{-1} in the watershed, with 36% of annual C productivity in leaf litter and 64% in wood growth (Smith et al., 2017). Smith et al. (2017) also showed that forest productivity varies across the watershed. Generally, productivity is greater on south aspects than north, greater in swales than planar slopes, and greater in the valley floor than ridgetops. Maximum tree growth happens in northern red oak (*Quercus rubra* L.) growing in swales. Understory shrubs are a very small component of the aboveground biomass (<1%).

Forest composition, productivity, and demographics have been measured in Shale Hills during two inventory periods (2008–2012 and 2012–2016), with a survey of the >2000 trees in the watershed that are >20-cm stem diameter. The most notable change between

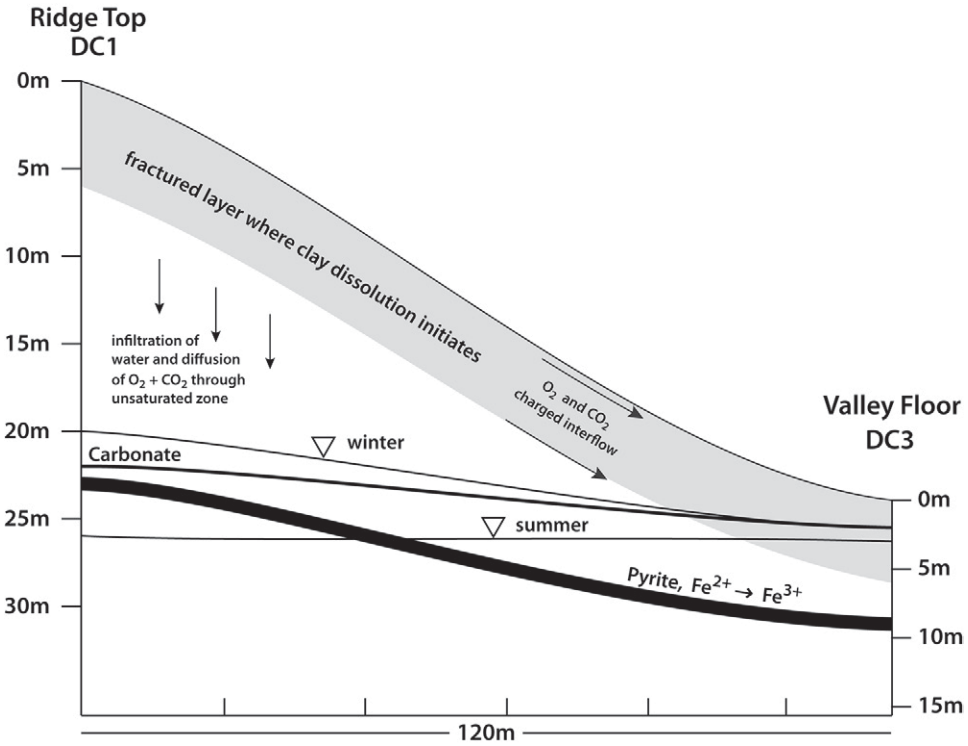

Fig. 4. Schematic cross-section showing the upper fractured layer, where feldspar and clay dissolution largely occurs, and the deeper reaction fronts for carbonate and pyrite. The carbonate front is relatively close to today's deep regional water table and is close in depth to the pyrite reaction front under the ridge, where it is hard to ascertain exact depths. The pyrite reaction front is deeper than today's water table under the valley, as shown. Above each reaction front, the mineral of interest becomes depleted. The upper layer of soil and highly fractured rock shown in gray allows lateral subsurface flow (also referred to here as interflow) of water. Most of the water that infiltrates at the land surface flows along this pathway or is lost to evapotranspiration, leaving relatively little water recharging the deep groundwater. Figure reproduced with permission from Brantley et al. (2013).

the first and second tree inventory periods in the watershed was an order of magnitude increase in tree mortality. Mortality of trees between 2008 and 2012 was 1.0%, while mortality from 2013 to 2017 was 9.8%. A small-scale wind blowdown in August 2017 caused 2.3% mortality of tree stems, which represents 3.0% of the basal wood area in the watershed. Prior to that blowdown, 142 of the 2068 trees surveyed died, which were 6.9% of the stems and 4.7% of the basal wood area.

The most common cause of mortality was non-native pests that killed all elms (100%), most of the ash (88%), and some American beech (25%). While none of these species are dominant in the watershed (Smith et al., 2017), their decline and loss represents a degradation of the richness of the forest. Furthermore, defoliation and mortality of many of the dominant species (e.g., oak and eastern hemlock [*Tsuga canadensis* (L.) Carrière]) are likely to accelerate due to invasive pests such as gypsy moth and hemlock woolly adelgid. The loss of such foundational tree species will affect C storage, evapotranspiration, and stream flow (Hadley et al., 2008; Clark et al., 2010). Finally, the recent uptick in tree death is attributed to global change (e.g., invasive species and extreme weather) and is consistent with the inference that mortality rates witnessed today may be higher than those during past CZ development. It is possible that future tree mortality may continue to increase with rising global change stressors.

Basic Long-Term Observations

Shale Hills was originally investigated using irrigation experiments in the 1970s long before the CZO program was initiated (Lynch, 1976). As shown in Fig. 5, a multitude of variables have been measured in the CZO at Shale Hills for many different purposes since 2007. These variables have been measured at multiple locations, by multiple investigators, using multiple pieces of equipment or techniques, for varying durations using varying time intervals. Supplemental Table S2 summarizes measurements and points to the online database, where this information is compiled. These measurements are discussed further below.

Stream discharge from Shale Hills has been monitored by the CZO team since 2006 with some hiatuses. From 2006 to 2012, a double V-notch weir was used to measure depth and convert it to stream discharge using a rating curve (Nutter, 1964). The weir deteriorated and no measurements of discharge were obtained between November 2012 and October 2015. For that period of time, modeling reanalysis information is now used to estimate discharge. In October 2015, a 76-cm (2.5-ft) fiberglass H-flume with a 228.5-cm (7.5-ft) three-dimensional approach was installed. Sensors in an attached stilling well now measure depth, water temperature, and electrical conductivity. Stream discharge is now calculated from the depth data.

Thirty-two wells are present in the catchment, spanning depths ranging from 1 to 35 m. Of these, the level and temperature of the groundwater are recorded in 13. Wells have generally been sporadically monitored, but more intensive measurements began in 2013. Where HOBO sensors are deployed, measurements are recorded at 15-min intervals and corrected to manual measurements.

Precipitation is measured using an Ott Pluvio weighing bucket located on the north ridge of the catchment. These measurements began in 2006 with a 10-min interval. A Laser Precipitation Monitor Disdrometer (LPM) was also coupled with the weighing

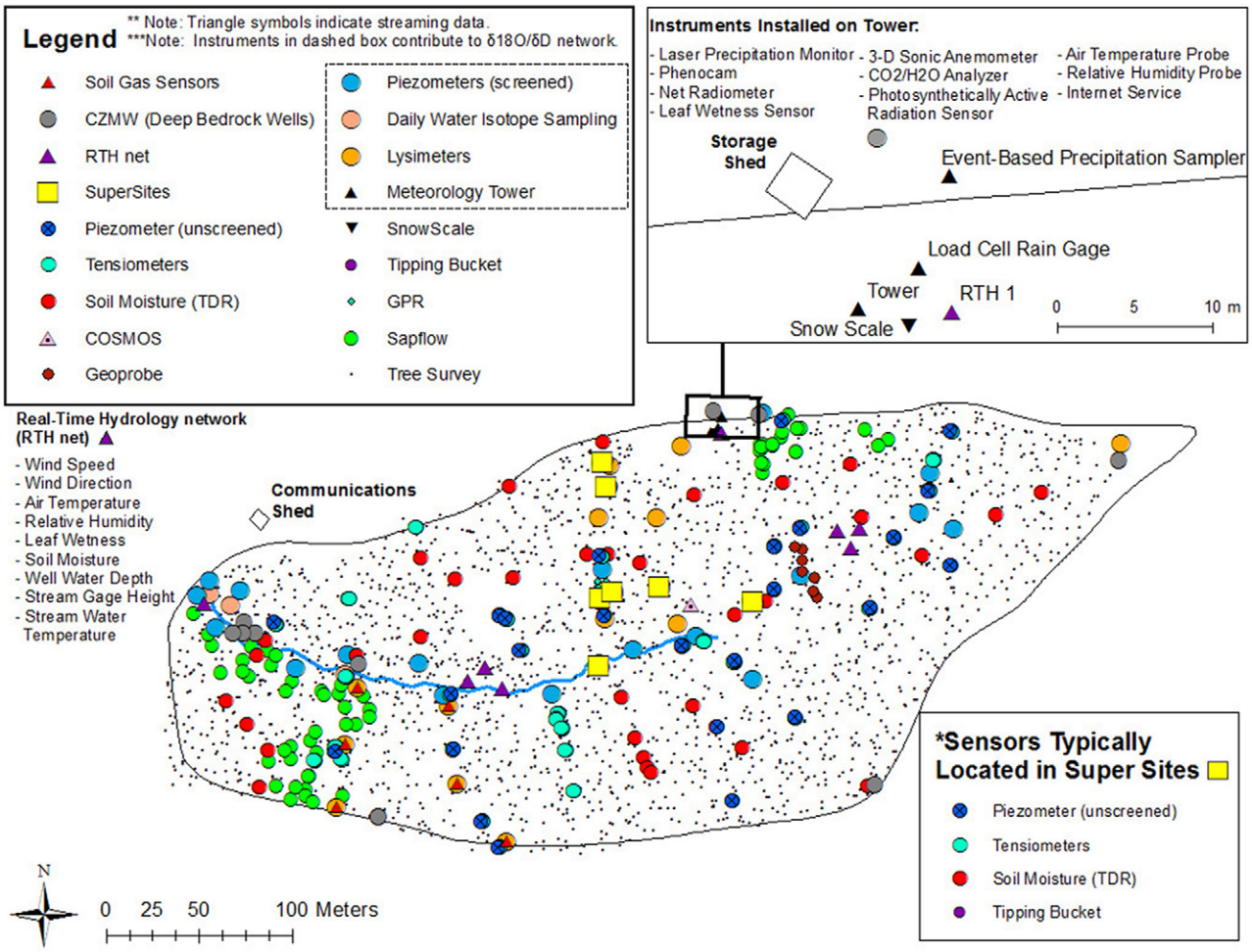

Fig. 5. Mapped summary of the currently deployed sensor network at Shale Hills (http://www.czo.psu.edu/data_overview.html).

bucket data from 2009 to 2014. Other tipping bucket precipitation gauges were used in six locations throughout the watershed from 2007 to 2014 to monitor local understory precipitation for a soil monitoring network operating at that time.

Air temperature and relative humidity measurements are made at the north ridgetop and in the valley bottom at the flume. These data are recorded at a 10-min interval and are streamed to the campus network.

Dedicated Long-Term Observations

There are many instruments deployed in the catchment for additional long-term observations (Fig. 5). The duration of individual sets of measurements vary because of funding constraints since inception of the CZO as well as equipment malfunctions or upgrades.

Eddy Covariance

A tower located at the top of the watershed (Fig. 5) measures land–atmosphere exchanges of water, energy, momentum, and CO_2. The measurements are continuous in time, and fluxes are estimated with a time resolution of 30 min. Sensible heat flux, evapotranspiration, momentum flux, and CO_2 flux are measured via eddy covariance. These represent Earth–atmosphere exchange over an area of roughly 1 km^2, but the size and location of this area varies with wind direction and atmospheric stability (Kljun et al., 2015). Total land–atmosphere exchange is measured.

While the turbulent flux measurements are valid as long as the sensors are functional, they only represent surface–atmosphere exchanges well when the turbulence is vigorous enough to make the atmospheric surface layer budget essentially one-dimensional (Yi et al., 2000), dominated by vertical exchange. This approximation is most often satisfied during daytime hours and in the summer. The tower instrumentation measures the turbulence intensity directly, thus screening algorithms can readily be constructed (e.g., Goulden et al., 1996; Barr et al., 2013). The method is also based on the assumption of steady-state atmospheric turbulence; non-steady conditions are screened using methodology reported in the literature (Vickers and Mahrt, 1997). Radiative energy fluxes are measured by a four-component radiometer that quantifies hemispherically integrated incoming and outgoing visible (solar) and infrared (terrestrial) radiation. These observations sense the area intersected by the hemispheric view of the instruments mounted on the tower.

Soil Moisture

Extensive monitoring sites for soil moisture include: (i) classical hydrometry with manual data collections, including multi-depth time domain reflectometry (Lin, 2006; Baldwin et al., 2017) and nested tensiometers (Yu et al., 2015), and (ii) automatic monitoring stations for real-time soil moisture and soil temperature (Lin and Zhou, 2008; Graham and Lin, 2011; Liu and Lin, 2015). Various manifestations of a vast soil moisture sensor network comprised of 35 sites distributed across the catchment were established since 2006 and 2011 (Liu and Lin, 2015).

Since 2015 we have focused on our four GroundHOG sites as described in detail previously (Brantley et al., 2016). GroundHOG, designed as a parsimonious way to monitor the CZ in a small catchment, consists of observation locations at ridgetop, midslope, and valley floor along a south hillslope transect plus a fourth site at midslope on a north hillslope.

At each GroundHOG site, a soil pit was excavated for soil profile description, soil sampling, and sensor installation. HydraProbe (Stevens Water Monitoring Systems) sensors were installed at depths of 10, 20, and 40 cm at each GroundHOG site to record soil moisture and soil temperature continuously at 10-min time intervals. In addition to point-based soil moisture data, areal-averaged soil moisture content has also been collected using a cosmic-ray soil moisture observing system since 2011. This unit has an effective horizontal footprint of ~300 m and a dynamic vertical measuring depth of 0.6 to 0.7 m (Zreda et al., 2012).

Lysimeters

Nested suction lysimeters have been used to collect soil pore water as described previously (Jin et al., 2011a). Soilmoisture 1900 series porous cup lysimeters are used (48-mm diameter, Soilmoisture Equipment Corp.). The current configuration of lysimeters is part of the GroundHOG design (Brantley et al., 2016). Specifically, lysimeter nests on the north-facing planar slope that we sample as part of the GroundHOG include the ridgetop, midslope, and valley floor positions, while on the south-facing slope, lysimeters are sampled only at the midslope. At all locations, we sample at depths of 20, 40, and D-20 cm, where D is the depth of refusal by augering. Many elemental and isotopic species have been analyzed and investigated in the soil lysimeter waters (Jin et al., 2011a; Yesavage et al., 2012; Thomas et al., 2013; Noireaux et al., 2014; Meek et al., 2016; Sullivan et al., 2016b).

Vegetation

Vegetation and aboveground biomass and C are measured and monitored in the Shale Hills watershed through a variety of approaches. All trees in the watershed >20-cm diameter are surveyed every 4 yr, initially in 2008 with reassessments in 2012 and 2016. This includes >2000 trees from 23 species, with each tree location mapped. During each survey, the trees are relocated, vitality and injuries noted, diameter measured, and crown class compared with the surrounding tree canopy assigned (dominant, codominant, intermediate, and suppressed). Trees passing the 20-cm-diameter threshold between surveys are identified as to species, tagged, mapped, and added to the survey database. In addition, approximately 100 trees have in-house fabricated dendrometers: these tight bands are fitted around the trunk to record annual and intra-annual diameter growth. Dendrometer data, measured annually in the fall at the end of growing season, complement the diameter measurements taken on all trees every 4 yr by adding high temporal resolution at a lower spatial extent. Survey and dendroband measurements are used to model biomass and C stored each year in aboveground wood. Additionally, leaf litter is collected each fall at 50 points across the watershed weekly or biweekly from September to December to measure annual leaf biomass. This biomass can be converted to annual leaf litter C input to the forest floor as discussed below.

Dedicated Campaigns and Experiments

The Carbon Budget

Many elements of the C budget have been measured in the watershed. Figure 6 presents our understanding of the annually averaged, watershed-integrated C balance. In the figure, a single value for each pool and flux is summarized, and the values are noted as to whether they are measured vs. modeled. Direct observations include both C pools and fluxes as described in the previous sections. The temporal and spatial coverage of the data are complex. Some values (e.g., soil organic C and root C) have been measured only once, at many points in space, and extrapolated to the watershed total. Others are measured periodically (aboveground C, aboveground net primary productivity, litter fall) at many points and extrapolated across the watershed. Some are measured frequently (net ecosystem productivity [NEP] and heterotrophic respiration) but are difficult to extrapolate across space or time and thus are not directly extrapolated to a watershed-integrated, annual value but instead are used to evaluate and calibrate our numerical modeling system, Flux-PIHM-BGC (Shi et al., 2018). The only observations that have been integrated into Flux-PIHM-BGC to date are aboveground net primary productivity (ANPP) and aboveground C (used to adjust the mortality rate). Net ecosystem productivity and soil C pools have been used to evaluate the modeling system, but no data assimilation has yet been performed. A more comprehensive assimilation of data from the entire watershed C cycle system is underway.

To calculate the C budget at the Shale Hills watershed, the coupled land surface hydrologic ecosystem biogeochemistry model Flux-PIHM-BGC (Shi et al., 2018) was used. Flux-PIHM-BGC couples a terrestrial ecosystem C–N model Biome-BGC (Thornton et al., 2002) and the Noah land surface model (Chen and Dudhia, 2001; Ek et al., 2003) to a physically based, spatially distributed hydrologic model, the Penn State Integrated Hydrologic Model (PIHM [Qu and Duffy, 2007]). Flux-PIHM-BGC also includes a topographic solar radiation module and an

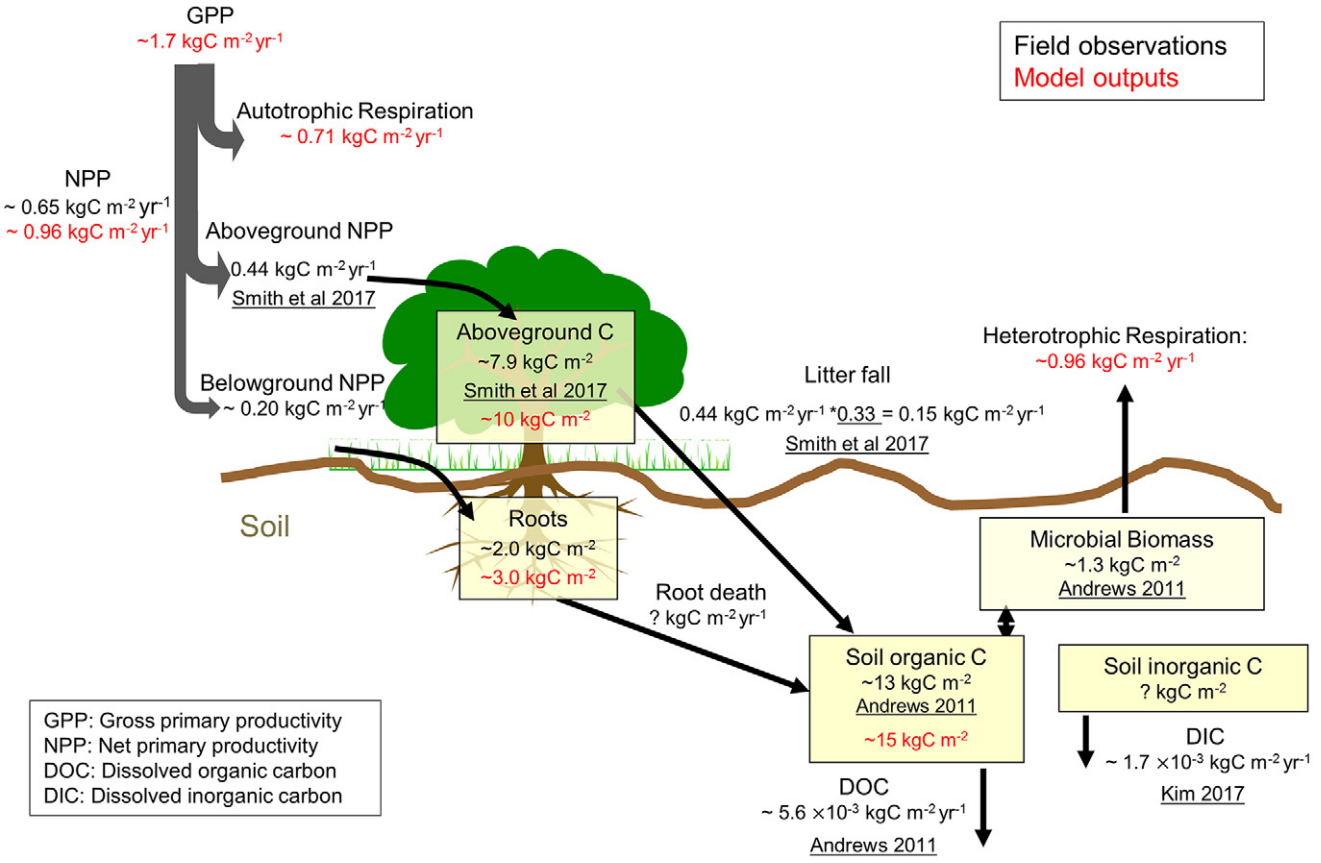

Fig. 6. Observed and simulated C budget at the Shale Hills watershed. The litter fall is estimated from data from Smith et al. (2017), where the leaf turnover rate is 0.33 and aboveground net primary productivity (NPP) is 0.44 kg C m^{-2} yr^{-1}. The model simulation was performed using Flux-PIHM-BGC for the time period between 2009 and 2011. The temporal domain of the observations varies. Kim (2017) was a personal communication.

advection-driven soil mineral N transport module. Both enhance the model's capability to represent the spatial variation of ecosystem processes.

For the Shale Hills simulation, a lidar-measured surface terrain map (Guo, 2010) and field-surveyed map of soil depth are used to describe the characteristics of the model domain. For the sake of simplification, uniform forest type is used and all model grids are assumed to be covered by deciduous trees. The soil hydraulic properties are supported by limited field measurements (Lin, 2006; Baldwin, 2011). The physical land cover properties are described by the default vegetation parameters as used in the Noah land surface model. The ecophysiological parameters for deciduous trees are obtained from the default Biome-BGC input file, except that the default annual whole-plant mortality fraction is replaced by the ratio of (observed annual aboveground productivity)/(observed aboveground biomass) (Smith et al., 2017).

The annual N deposition rate is obtained from the National Atmospheric Deposition Program Leading Ridge site located near Shale Hills within the Shaver's Creek watershed. In situ meteorological forcing time series of precipitation, air temperature, relative humidity, wind speed, and surface pressure are applied. Downward longwave radiation and direct and diffuse solar radiation (for topographic solar radiation) are obtained from the Surface Radiation Budget Network (SURFRAD) Penn State University station. The land surface and hydrologic parameters are manually calibrated (i.e., trial and error [Shi et al., 2013]) using discharge, groundwater level near the stream, sensible and latent heat flux observations from the eddy covariance flux tower, and cosmic-ray soil moisture observing system measurements. The C budget was simulated from 1 Jan. 2009 to 1 Jan. 2012 after a 500-yr accelerated decomposition spin-up and a 500-yr native model dynamics spin-up.

The observed and simulated C budgets shown in Fig. 6 are similar, with the exception of ANPP. Modeled ANPP is notably larger than observed ANPP. We are in the process of comparing observed and modeled heterotrophic respiration and daytime NEP to investigate this discrepancy. Uncertainties in both modeled and observed fluxes and pools are difficult to quantify, making it difficult at present to evaluate the significance of the model–data differences. Annual NEP is not currently available from either the model (run to equilibrium) or the observations. Annual NEP cannot be quantified from observations because the complex terrain prevents a reliable annual sum from being computed from the flux measurements, and heterotrophic respiration measurements have not been extrapolated across space and time to close a component flux budget.

The Nitrogen Budget

As shown in Fig. 7, Weitzman and Kaye (2018) constructed a N budget from a compilation of field measurements and relationships established in the literature (e.g., the ratio of N_2/N_2O loss in temperate forests). Recent rates of annual N deposition are 3 to 5 kg N ha^{-1} yr^{-1} in precipitation (National Atmospheric Deposition Program, 2016) and 1 to 2 kg N ha^{-1} yr^{-1} in particulate matter (CASTNET, 2016). This is consistent with observations in much of the northeastern United States, i.e., that wet and dry deposition of N increased to a peak of 11.5 kg N ha^{-1} yr^{-1} in the mid-1990s and has steadily declined to the present. Even after decades of anthropogenically elevated N deposition to the forest, the watershed remains a strong sink for N, retaining more than half of inputs. Gaseous losses from the soil surface appear to be the largest output of N (20× larger than stream exports).

It is possible that unmeasured losses (e.g., denitrification in groundwater) account for some of the discrepancy between inputs and outputs (>4 kg N ha^{-1}), but an alternative explanation is that N is accumulating in the soil or trees. Due to the high spatial variability in soil N and bulk density, we have not attempted to measure changes in soil N with time. We have, however, found that the trees take up a very large flux of N—perhaps between 9 and 18 kg ha^{-1} yr^{-1}. This tree N uptake surprised us because the canopy-dominant trees in the forests are ~120 yr old, and we expected the tree N pool to be at steady state. Trees may still be mining N from the soil, leaving behind soil that can take up more N (Johnson, 1992).

Several characteristics make this Shale Hills N budget distinct from other eastern deciduous forests (Weitzman and Kaye, 2016, 2018). First, most well-studied eastern forests (e.g., Hubbard Brook) do not have N inputs from rocks, while at Shale Hills ~12% of N inputs derive from weathering of the shale. In some California watersheds, inputs of bedrock N can lead to soil N saturation (Dahlgren, 1994), but our observations here show that N-bearing rocks do not always saturate soils in N; in addition, millennia of small N inputs from rocks do not necessarily lead to high stream water N losses.

A second distinct feature of our N budget is the high measured N_2O and calculated gaseous N losses. Other well-studied forests that are estimated to be "N saturated" have much lower N_2O losses than Shale Hills. We have speculated that the intermediate clay content (~20%) at Shale Hills may lead to microsite heterogeneity (Castellano et al., 2010) that promotes N_2O losses.

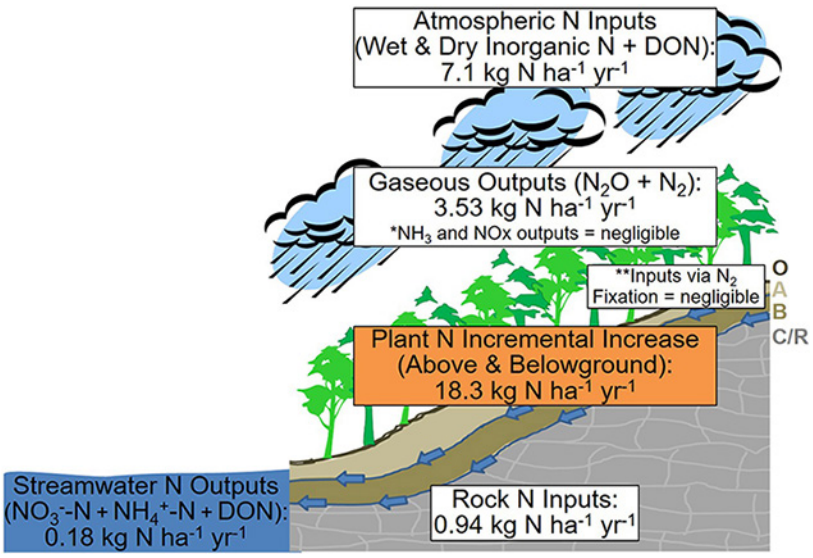

Fig. 7. Nitrogen budget of the Susquehanna Shale Hills Critical Zone Observatory depicting the main atmospheric N inputs, stream water and gaseous N outputs, and the recycled plant N pool. Figure reproduced with permission from Weitzman and Kaye (2018).

The Water Budget

Even though the water budget is the most intensively studied mass balance in Shale Hills, it is not possible to measure the complete water budget. We therefore use a synthesis of observations and numerical modeling (Shi et al., 2015) to construct as complete a picture of the water budget of the system as possible. The observations provide the foundational data on which the budget is constructed. The numerical modeling system provides the interpolation in time and space needed to extend the measurements across the watershed using our understanding of the governing equations. This type of numerical "reanalysis" is well established and widely used in the atmospheric sciences (Kalnay et al., 1996). Model–data synthesis enables quantitative evaluation of hypotheses concerning the function of the water cycle, as well as the creation of a "best guess" water budget that can be used to support the study of other cycles and processes that depend on the water cycle.

Figure 8 shows the water budget of the watershed, including both observed and modeled components and, when available, our understanding of the uncertainties in these quantities. The Penn State Integrated Hydrologic Model with a deep groundwater (DGW) module has been used to calculate the water balance. PIHM-DGW was developed to add the representation of deep groundwater to PIHM. When a fractured bedrock layer is present, groundwater in the soil layer can infiltrate into the bedrock layer. When the level of deep groundwater is higher than the depth to the bedrock layer, i.e., the soil transient groundwater and the deep groundwater are connected, excess deep groundwater becomes transient groundwater. For the Shale Hills simulation, a head of 270 m is applied as the boundary condition for deep groundwater at the model grid with the highest elevation, as suggested by Sullivan et al. (2016a). For the fractured bedrock layer, hydraulic properties are assumed to be uniform in the watershed. The bedrock vertical and horizontal hydraulic conductivities are parameterized to be 1/100 of the corresponding values of the Weikert soil type, which covers most of the spatial area of the subcatchment. The bedrock porosity is set to 1/10 of the Weikert soil porosity. The van Genuchten parameters for fracture (α = 10.0 m^{-1}, n = 2.0; Gerke and van Genuchten, 1993) are used.

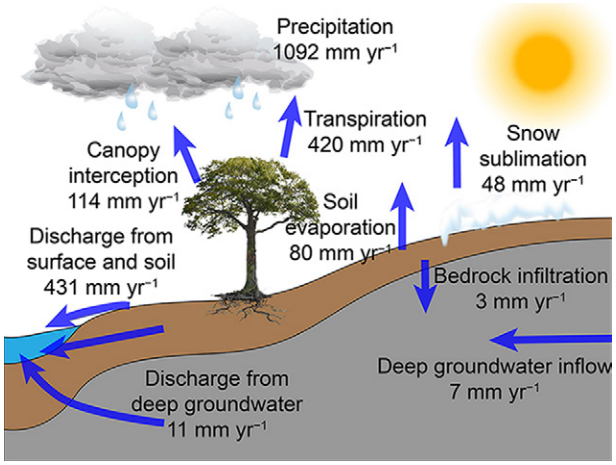

Fig. 8. Annual water balance between 2009 and 2011 as simulated using Flux-PIHM-DGW.

As shown in Fig. 8, the catchment on average receives approximately 1 m yr^{-1} as rainfall, and about 40% of this influx infiltrates and leaves through the stream or as groundwater. With this simulation it was also necessary to infer an influx from deep groundwater that makes up 1% of the precipitation influx.

Understanding Temporal-Spatial Patterns of Water

We can also look at detailed hydrological processes using data and model output for specific time intervals as shown in Fig. 9 for 1 Apr. to 31 Dec. 2009. Shale Hills subcatchment is hydrologically responsive, with stream discharge closely following intensive precipitation events. During the time interval shown, the total precipitation was 0.9 m. Total evapotranspiration (ET) increases from spring to summer and then decreases in winter. Although the precipitation is relatively invariant during the year, water storage decreases in the summer due to high ET, as observed in the water level drop in monitoring wells (Shi et al., 2013). The model shows that 39.7% of the annual precipitation contributes to stream discharge and 58.8% to total ET, with the remaining 1.5% as water storage. Watershed-averaged variables were calculated by summing up grid-scale daily modeling output and averaging by the watershed land surface area.

Field observations indicate strong evidence of deep groundwater flow into the stream, with chemical compositions different from those of the soil water (Jin et al., 2011a, 2014; Thomas et al., 2013; Li et al., 2017a). The unmeasured value of the groundwater influx (Q_G) was tuned to 1.04×10^{-4} m^3 m^{-2} d^{-1} to reproduce the stream chemistry, as discussed below. This water flux is 6.7% of the calculated 0.015 m^3 m^{-2} d^{-1} of average stream discharge in 2009.

As shown in Fig. 9B, the contribution of different flows varies significantly depending on hydrological conditions. During rainfall events, surface runoff (Q_S) dominates as short-lived pulses in early stages. The Q_S is followed by subsurface lateral flow (Q_L) with a longer time duration. In the summer, when more water is lost through ET, the stream discharge is dominated by Q_G, providing base flow. During most of the year, however, Q_L contributes >70% of the discharge (see also Fig. 4). This is consistent with tracer and groundwater table data indicating that contributions to the stream derive mainly from groundwater during warm periods (low discharge) and from soil water during cold periods of high discharge (Jin et al., 2011a, 2014).

Atmospheric Inputs of Metals: Manganese

Manganese cycling in the Shale Hills subcatchment reflects the combined influences of atmospheric deposition and plant uptake (Fig. 10). Shallow soils throughout the catchment are highly enriched in Mn, and ~50% of all Mn contained in ridge soils is derived from atmospheric deposition (Herndon et al., 2011). Current rates of Mn and Pb deposition are low compared with those that occurred during a period of heavy regional industrialization from the mid-19th to mid-20th centuries (Ma et al., 2014). Other metals have also been deposited (Kraepiel et al., 2015). Many shallow soils throughout Pennsylvania and the northeastern United States are similarly enriched with Mn (Herndon et al., 2011), indicating widespread soil contamination from industrial sources. Although Mn is readily solubilized from the acidic soils within the subcatchment, leaching of Mn from soils and transport into the stream is slowed by rapid cycling through vegetation (Herndon et al., 2015b). Specifically, the annual rate of Mn uptake by forest vegetation exceeds the rate at which Mn is leached from ridge soils by >20×. Although Mn is eventually returned to the soil in leaf litter, the Mn that is stored in biomass is oxidized and immobilized as Mn oxides during litter decomposition (Herndon et al., 2014). Consequently, only low concentrations of dissolved Mn are leached from ridge and planar soils each year. However, organic-rich swales contain high concentrations of dissolved Mn that are delivered to the stream (Herndon et al., 2015b). Enriched Mn dissolved in swale pore waters derives from accumulated Mn-rich soil organic matter in those zones of convergent water flow (Andrews et al., 2011; Herndon et al., 2015b). Observations made at Shale Hills indicate that biological cycling increases Mn retention in ecosystems impacted by industrial inputs, and Mn is only gradually released from soils into streams.

Understanding Concentration–Discharge Relationships

Understanding concentration–discharge (C–Q) relationships of solutes in streams has become a focus of watershed hydrology. In Shale Hills, measurements and models show that whether a given solute concentration changes very little during orders-of-magnitude changes in discharge—so-called *chemostasis*—or they show dilution or some other type of behavior, the underlying reasons can be variable and complex.

At Shale Hills, geogenic species (Na, K, Mg, and Si) deriving from soil weathering exhibit chemostatic behavior. In contrast, the C–Q relationship of bio-relevant species (Ca, Mn, Fe, and dissolved organic C) are chemodynamic, with concentrations decreasing

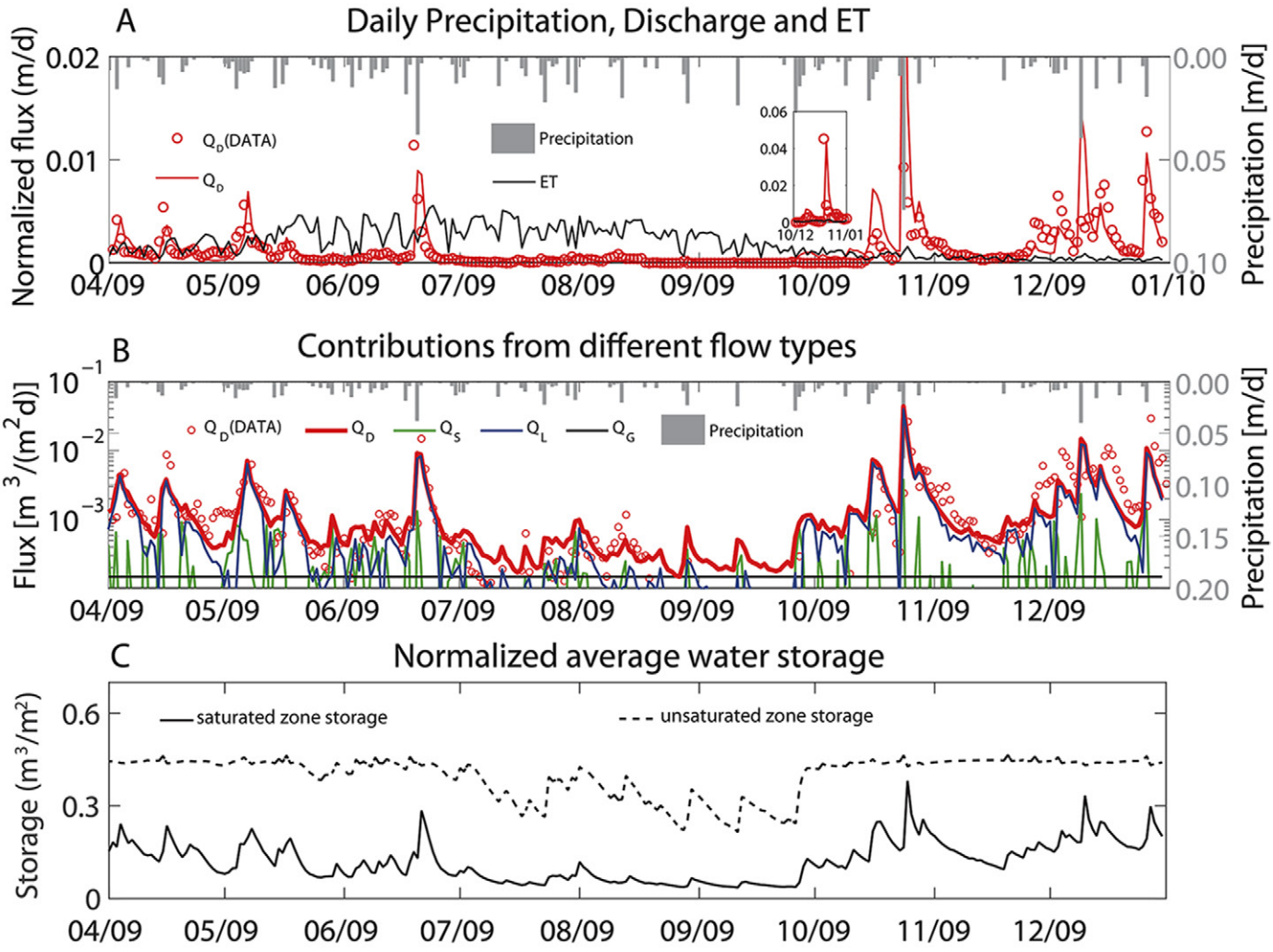

Fig. 9. (A) Temporal evolution of measured daily precipitation (m d^{-1}), discharge Q_D (m d^{-1}), and total evapotranspiration (ET (m d^{-1}), all normalized by land surface area. (B) Contributions to stream discharge (Q_D) are shown from different flows: surface runoff (overland flow) (Q_S), lateral subsurface flow (Q_L), and groundwater influx (Q_G). Note that under low-flow conditions, Q_S and Q_L values are $<10^{-4}$ m d^{-1} so they do not show up in the figure. (C) Temporal evolution of water storage in the saturated and unsaturated zones (m^3 m^{-2} land surface). Daily water storage varies seasonally: water storage is higher because of lower ET in spring and winter and is lower because of higher ET in the summer. The model output shows that water storage in the saturated zone is responsive to rainfall events, indicating that rainfall events primarily raise the shallow water table and increase the thickness of the saturated zone (Li et al., 2017a).

with increasing discharge (Herndon et al., 2015a, 2018). This has been explained by the differences in their sources and spatial distributions. Soil minerals are abundant and are homogeneously distributed throughout the subcatchment, whereas soil organic C is not (Andrews et al., 2011). Solutes that are involved in biotic cycling (Mn, Ca, and K) or that form strong complexes with dissolved organic C (Fe and Al) therefore exhibit similar patterns as the dissolved organic C. Dissolved organic C in rainfall that falls on the subcatchment also varies with time (Iavorivska et al., 2017).

As described above, the hydrologic model Flux-PIHM has been used to understand these C–Q relationships (Fig. 11). A newly developed reactive transport module (RT) has been added to the code: RT-Flux-PIHM was used to explore the chemostatic behavior of Cl and Mg (Bao et al., 2017; Li et al., 2017a). Simulation results show that the dry conditions in the summer allow only low flow from a relatively small connected hillslope area to the stream, leading to Cl trapped mostly in unconnected planar slopes. Large rainfall events that wet and connect a much larger portion of the watershed flush out the trapped Cl and counteract the dilution effects brought by the high water volume. These interdependent hydrological flow and Cl mobilization phenomena lead to Cl chemostasis.

Simulation results also indicate that Mg chemostasis is maintained by the synchrony between soil water content, lateral subsurface flow (interflow), and clay dissolution as the Mg source. The mass flux in stream discharge is dominated by interflow (Q_L), which flushes dissolved Mg from ion exchange sites in the soil and is responsive to surface hydrological conditions. Simulation results show that the surface area of dissolving clays in contact with flowing water (A_W) increases proportionally to the soil water content (V_W) and lateral flow Q_L. Chemostasis for Mg is thus largely dictated by the roughly constant A_W/V_W ratio

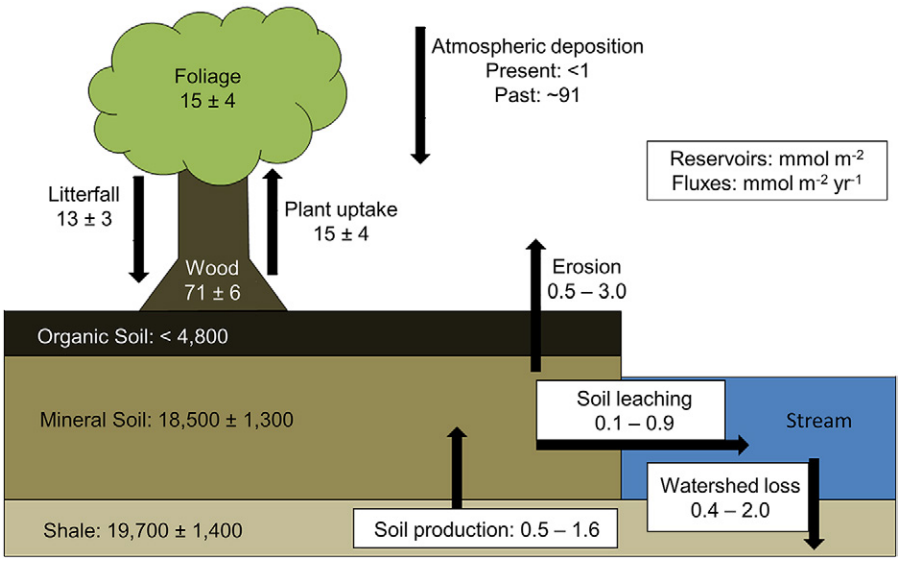

Fig. 10. Reservoirs (mmol m^{-2}) and fluxes (mmol m^{-2} yr^{-1}) of Mn quantified for Shale Hills. Fluxes of Mn between reservoirs are indicated by arrows, and values or ranges of values for each flux are displayed in white boxes. Ranges of values are given in cases where large spatial heterogeneities in fluxes were estimated. Today, Shale Hills is a net exporter of Mn when watershed outfluxes rise above 1 mmol m^{-2} yr^{-1}. Figure reproduced with permission from Herndon et al. (2015b).

under varying hydrological conditions. In the dry summer, low water content leads to small A_W and therefore slower clay dissolution. Large rainfall events increase V_W, Q_L, and A_W, therefore dissolving more clay and compensating the dilution effects brought by rainfall. This synchrony reflects the responsiveness of clay dissolution to hydrological changes. Sensitivity analyses discussed by Li et al. (2017a) show that Mg influxes cannot be derived primarily from relatively constant deeper groundwater fluxes because if they are unresponsive to surface hydrological conditions then dilution behavior would occur instead of chemostasis (Fig. 11).

Data and Collaboration

Data Management and Policy

Three data types are collected at SSHCZO and used along with model outputs to understand the system. First, sensor data are transmitted directly from the field to the campus computer network, where they are processed. Second, samples are collected manually by investigators and students and brought back to the laboratory for analysis. Third, some measurements are made in the field on rock structures or landscape features. Finally, reanalysis "data"—model outputs—are derived from numerical simulations using available datasets and other data as needed.

Data are available under the sharing practice defined below through a web interface within embargo limitations (generally within 2 yr of measurement). Sample data are available on the SSHCZO data website and are stored and archived in database and flat files.

Data Sharing

All SSHCZO investigators and collaborators who receive CZO support agree to share data privately within the CZO team within 1 yr. The CZO investigators and collaborators agree to provide data files and metadata for raw, quality controlled and/or derived data to CZO data managers within 1 yr of collection. By default, data values are held in password-protected directory/files, but metadata are made public with full attribution to dataset creators. The CZO investigators also agree to release data publicly after 2 yr, but many choose to release data sooner. In unusual cases, scientists extend data privacy beyond 2 yr to protect student theses,

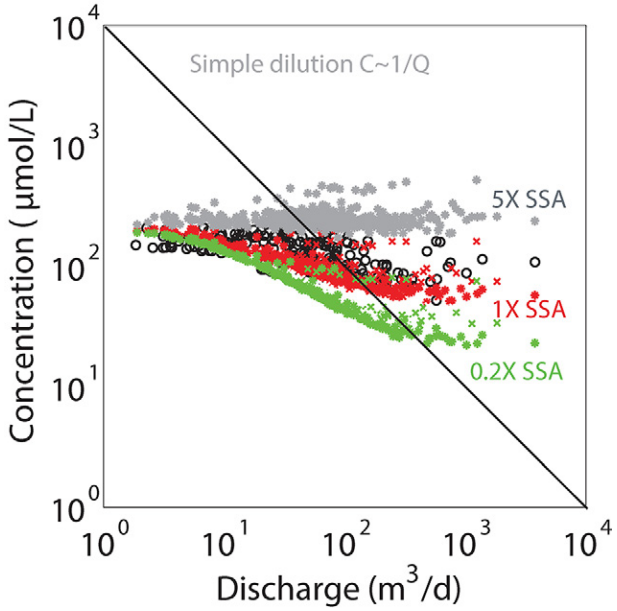

Fig. 11. Magnesium concentration–discharge (C–Q) relationships explored with model simulations calculated for different assumptions of the mineral specific surface area (SSA). The black dots are data. The red dots are output from the best-fit model of RT-Flux-PIHM with calibrated SSA and cation exchange capacity (CEC) (labeled 1X SSA). The gray and green dots are model output when setting the SSA five times larger (5X SSA) and five times smaller (0.2X SSA), respectively. We have inferred from the figure that a larger dissolving mineral surface area leads to more chemostatic behavior because the Mg mass flux into the stream primarily derives from dissolution of chlorite in the shallow soil zone—i.e., hydrologically responsive interflow—under all conditions of discharge. At low SSA (0.2X SSA), in contrast, the Mg mass flux from groundwater becomes more important, and dilution behavior occurs under high discharge conditions as more water dilutes the constant Mg input from groundwater.

but this is discouraged. All investigators are encouraged to consult with creators of CZO datasets prior to use.

The data policy on the SSHCZO data website emphasizes free use of all CZO data. All CZO data products except those labeled private may be freely copied, distributed, edited, etc., as long as acknowledgment is given.

New Insights and Scientific Findings

Five working hypotheses have emerged from the SSHCZO.

Hypothesis 1

We hypothesize that in humid temperate forests, water is mostly taken up into trees from the upper 30 cm of soil; at the same time, nutrients are mostly foraged by roots of trees with arbuscular mycorrhizal fungi—especially in trees with thin roots—but by fungal hyphae in trees with ectomycorrhizal fungi—especially in trees with thick roots.

Tree species in humid forests such as those in the SSHCZO differ in fundamental ways with regard to water use and nutrient acquisition. The dominant tree genera, oaks and hickories, have a ring-porous vascular architecture and are more able to sustain sap flux and associated photosynthetic activity during the summer in dry years than the less drought-hardy maples and tulip poplars (Meinzer et al., 2013). The oaks and hickories also tend to be deeper rooted and are capable of using deeper sources of water than the maples (Gaines et al., 2016b). However, in the mostly moist summers, both oaks and maples tend to predominantly use relatively shallow sources of moisture (<30 cm deep), and water residence times tend to be short (Gaines et al., 2016a). These genera also differ fundamentally in their fine, absorptive root systems. The oaks and hickories are ectomycorrhizal and rely heavily on their fungal symbiont for nutrient acquisition (Chen et al., 2016, 2018). In contrast, the roots on the maples and tulip poplars host arbuscular mycorrhizas. The maples primarily forage with their thin roots in nutrient patches following a perturbation (e.g., tree death or mammal burrowing). Thick-rooted, arbuscular mycorrhizal species like tulip poplar tend to depend more on mycorrhizas as indicated by heavy colonization but are not very opportunistic with either their roots or fungi in nutrient foraging (Chen et al., 2016, 2018). Thus, the diversity of species in the Shale Hills catchment also reflects diverse strategies for acquisition of water and nutrients. An extensive measurement of root density completed in soil pits trenched into the shale showed that although the root density is highest near the land surface, roots also grow into the underlying shale rock (Hasenmueller et al., 2017), as shown in Fig. 12. Such data will allow a better understanding of why roots grow into rock even in temperate forested regions.

Hypothesis 2

The critical zone acts as a capacitor for atmospheric pollutants deposited at the land surface: N, S, Mn, Pb, and a few other metals have been deposited from different human activities during different time periods and now are leaving the CZ after different time lags.

Globally, many soils are enriched in elements that were emitted to the atmosphere as industrial byproducts; however, little is known about how long these contaminants persist in soils. The CZ can act as a "capacitor" for atmospheric deposition by temporarily

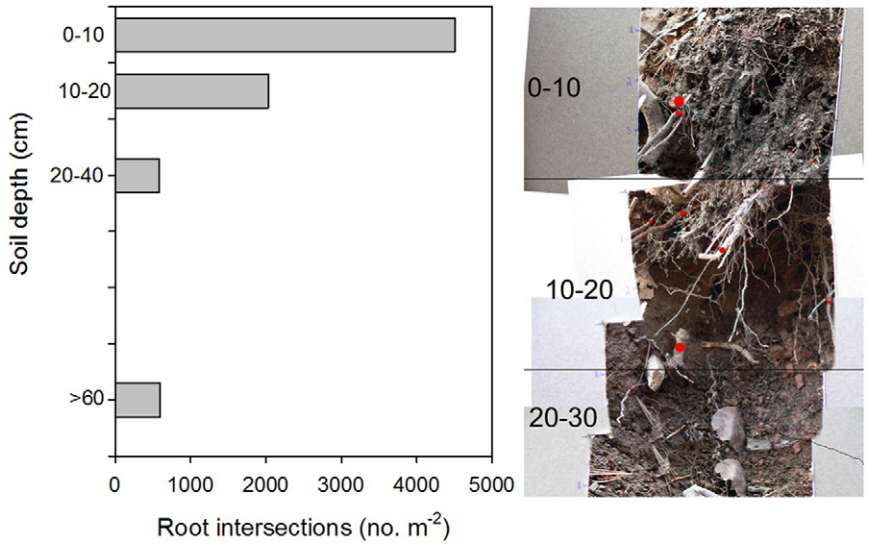

Fig. 12. Root distribution on a shale hillslope, showing the number of root intersections per square meter as a function of soil depth, averaged across three landscape positions (valley floor, midslope, and ridgetop) as described by Hasenmueller et al. (2017); root intersections were measured using high-definition photographs of the root pit walls using an Olympus STYLUS TG-860 Tough camera (Olympus Corporation) and custom-made mount, while the absolute root distribution was determined by counting every root intersection of an imaginary plane in transects of 10 by 30 cm—proportional to root length density assuming that roots are randomly distributed (Böhm, 1979); the values are the average values of eight transects in each pit, one pit at each landscape position (left). Example of photographs of a vertical transect in a midslope soil pit, with red dots indicating where roots intersect the plane; only photographs to a depth of about 25 cm are shown for illustration of the approach (right). Many red dots are not resolvable in this image without magnification.

storing contaminants and releasing them gradually with time (Herndon and Brantley, 2011). The duration of time between deposition at the land surface and removal from a catchment (its time lag) is unique for each contaminant and depends on hydrology, vegetation, and soil composition.

For example, surface soils in Shale Hills are enriched in Mn, Pb, Mo, Cd, Cu, and Zn due to past atmospheric deposition from anthropogenic sources such as coal combustion and iron furnaces (Herndon et al., 2011; Ma et al., 2014; Kraepiel et al., 2015). As discussed above for Fig. 10, relatively small quantities of dissolved Mn are leached from soils and exported in the stream each year. Processes described here all contribute to the ~20-yr lag time between the peaks of atmospheric deposition and riverine export into the Susquehanna River Basin (Herndon and Brantley, 2011) (Fig. 13). In comparison, biocycling has little influence on Pb and Mo, which instead are retained in soils through complexation with soil organic matter (Ma et al., 2014; Kraepiel et al., 2015). These findings reinforce the importance of plant–soil interactions in controlling the export of certain contaminants either directly due to intense biocycling (e.g., Mn) or indirectly due to contributions of soil organic matter (e.g., Pb and Mo).

Similar processes within the Shale Hills catchment probably influence cycling of N and S, which have been extensively deposited to watersheds across the northeastern United States in acid rain. As discussed for N above, atmospheric deposition has decreased following declines in emissions from fossil fuel combustion, but watersheds store legacy N and S that continue to be slowly released with time. Sulfate time lags depend on interactions between soil properties (clay content and soil depth) that control watershed storage capacity and hydrologic factors (discharge/precipitation ratios) that determine how quickly sulfate is flushed out of soils (Rice et al., 2014). In forest soils, N (as NH_4^+ and NO_3^-) can be retained for short times by abiotic interactions with soil organic matter and at longer timescales by root uptake that incorporates N into plant biomass (Weitzman and Kaye, 2016).

Hypothesis 3

The shaded sides of catchments in the northeastern United States are steeper than the sunny sides because the faster freeze–thaw cycling on the high-insolation sides drive more efficient downslope soil transport.

Many of the geomorphic, geochemical, and hydrologic observations of Shale Hills suggest that aspect exerts significant control on CZ processes at this site. The most fundamental observation of this control is the pronounced asymmetry between the slopes of the north and south walls of the catchment. Within Shale Hills and its adjacent watersheds, south slopes are consistently steeper than their northern counterparts (Jin et al., 2010; Ma et al., 2013; West et al., 2013, 2014). Similarly, there are consistent differences in soil thickness, where south slopes are mantled with generally thicker soils than the north slopes (West et al., 2014). Isotopic measures of soil weathering and erosion suggest that aspect exerts control on the evolution of the observed topographic asymmetry.

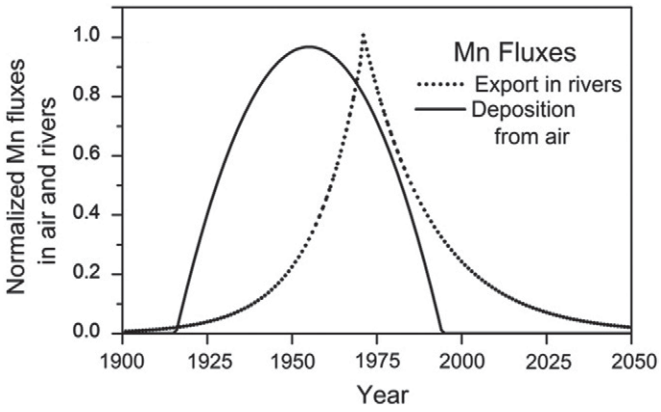

Fig. 13. Fits to atmospheric Mn deposition and riverine Mn flux data indicate a lag time of approximately 20 yr between the peaks of Mn deposition and riverine export in central Pennsylvania. Figure reproduced with permission from Herndon and Brantley (2011).

Interestingly, meteoric ^{10}Be-derived measures of downslope soil flux reveal that despite differences in hillslope gradient and soil thickness, mass fluxes of soil off the north and south slopes are equal. This requires that the efficiency of soil transport is a factor of two higher on north slopes than south slopes. After considering possible transport mechanisms that are strongly controlled by hillslope aspect and thus differences in solar insolation, we concluded that the probable transport mechanism responsible for the difference in transport efficiency at Shale Hills is frost heave. Measured soil temperatures reveal twice as frequent freeze–thaw cycles on north slopes than south slopes (Lin, 2014). This all implies that over geologic time, feedbacks in the weathering and erosion system may have driven topographic asymmetry to develop in response to differences in incoming solar radiation, maintaining a balance in material loss out of the watershed.

Hypothesis 4

The deepest of the nested reaction fronts under the valley, oxidative dissolution of pyrite, weakens the rock, accelerates stream incision, and leads to a cascade of shallower reactions that remove solutes and particles.

As shown in Fig. 4, the deepest reaction under the catchment outlet is pyrite oxidation. As pyrite oxidizes, it releases H_2SO_4 that dissolves and weakens rock nearby. Sullivan et al. (2016a) hypothesized that this chemical weakening of rock under the outlet was the first in a cascade of reactions that drove erosion of the catchment. According to Sullivan et al. (2016a), oxygenated waters flowed down both hillsides within the upper fracture zone (Fig. 4), oxidizing the pyrite beneath today's water table. As carbonates in the subsurface and other minerals are dissolved in the H_2SO_4, the water table at the outlet lowers slightly. In turn, the lowered water table may drive drainage from the hillslopes, in turn driving weathering high in the watershed, somewhat akin to a coupled incision–drainage model in the literature (Rempe and Dietrich, 2014). According to this hypothesis, incision in Shale Hills is controlled by the rate of delivery of oxygenated waters to the pyrite at

depth beneath the outlet. Pyrite oxidation is detected in the stream chemistry during some times of the year (Jin et al., 2014).

Hypothesis 5

Hillslopes connect to the stream along variable flow pathways dictated by inherited structural features and by emergent permeability contrasts that are recorded (or possibly caused) by reaction fronts.

Interflow, which annually contributes most of the stream flow in Shale Hills (Li et al., 2017a), is defined here as the subsurface, laterally flowing water that moves along permeability boundaries above the regional groundwater table before flowing into the stream (Fig. 4). Interflow moves seasonally through macropores and along soil horizon interfaces and rock fractures during wet periods and can be conceptualized as occurring within a zone of water saturation perched above the regional water table (Lin et al., 2006; Sullivan et al., 2016a; Nyquist et al., 2018). Interflow is dominated largely by water in swales during dry periods but includes both swale and planar hillslopes in wet periods. Stream flow becomes intermittent during dry conditions in late summer as evapotranspiration removes water from catchment soils and inputs from interflow and groundwater to the stream both decline. As storms occur and soils saturate, lateral flow through soils and fractured material along the nominally planar hillslopes becomes more and more common, eventually connecting the planar hillslopes to the stream.

Connectivity between these water sources is controlled by both structural features largely inherited from the bedrock and emergent features that develop in regolith by weathering. Inherited features include bedding-parallel fractures and protolith porosity, whereas emergent features include fracturing from frost-related processes as well as permeability variations caused by porosity changes induced by weathering (Fig. 4). In the eastern portion of the subcatchment, the protolith is almost completely low-permeability shale, and this explains the perched water table that allows interflow to deliver water to the channel within a relatively short residence time. Higher permeability sandstone layers become more prevalent in the western portion of the subcatchment, and they facilitate faster infiltration to the regional water table near the outlet.

Figure 14 summarizes the locations of the important reaction fronts and water flow paths under the ridges in Shale Hills. Brantley et al. (2017a) argued that sharp reaction fronts are often colocated at zones of permeability contrast. These contrasts explain why intermittent perched water tables and subsurface lateral water flow occur even in the largely unsaturated zone above the regional water table in a catchment on low-permeability rock such as Shale Hills. As shown in Fig. 14, the illite reaction front is colocated with the zone of interflow, while the carbonate and pyrite reaction fronts are colocated with the zone of lateral groundwater flow. Where water flow is more dominantly vertical, wide reaction fronts form such as the chlorite front shown in Fig. 14. These observations highlight the idea that knowledge of the distribution of geochemical reaction fronts could be used to inform better models of subsurface water flow paths.

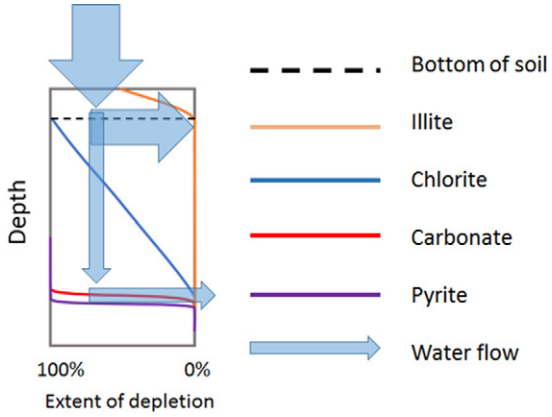

Fig. 14. A schematic diagram showing the dominant flow pathways for water and the depth intervals of four major reactions (i.e., the reaction fronts) hypothesized for profiles under ridgetops at Shale Hills. Most of the water (blue arrows) leaves the catchment in the upper 5- to 8-m-thick layer of fractured rock and soil (see also Fig. 4). Only a small fraction percolates to the deeper groundwater table, where it also flows laterally out of the catchment. The lateral water flow at shallow depths results from transient water saturation at zones of permeability contrast. Such permeability contrasts may often be colocated with sharp reaction fronts as shown (Brantley et al., 2017a). The two deepest reaction fronts are those of pyrite and carbonate minerals. The depths of these are hard to determine: the two fronts may exactly overlie one another or one may be deeper as shown. The blue and orange lines denote the reaction fronts for chlorite and illite. Pyrite, carbonate, and illite are lost over narrow depth intervals (sharp reaction fronts) but chlorite is lost over a wide depth interval (wide reaction front). The dashed line indicates the depth of augerable soil (this depth is only tens of centimeters and the figure is thus not to scale).

Precepts for Collaboration and Summary of Outreach

Collaborative Agreements

Collaborations across disciplines and time are complex, and we have used our experiences to develop "best practices for collaboration" for all students, faculty, and staff working at the CZO. Both the scope (what are the issues) and the guidelines for best management were developed iteratively in group meetings, and it remains a "living" document that adapts to changes in our team (bit.ly/SSHCZO_Collaboration).

The key topics covered are authorship; field infrastructure; collecting, sharing, and archiving samples and data; project management; advising students; outreach; and reporting. For example, in the section on authorship, we describe the criteria for authorship and answer questions that represent real cases that scholars encounter. Having a best practices document to address such questions has not prevented problems from occurring (nor did we expect it would), but it has reduced the number of conflicts and provided level-headed guidance in resolving conflicts that arise.

Outreach

Since its inception, the SSHCZO has educated 118 funded students and postdoctoral scholars, trained more than 100 visiting scholars, engaged 111 TeenShale Network high school participants, graduated 15 Master of Science and 13 Doctor of Philosophy

students, presented 140 student papers at national or international meetings, mentored 19 undergraduate thesis projects, funded eight seed grants for complementary research, and provided logistical support for more than five self-funded outside research grants.

Future Perspectives

Humans are changing the CZ at geologically unprecedented rates. Maintaining CZ services requires that we learn to project changes in the Earth's surface across space and time. In the SSHCZO project, we measure and model the landscape to learn to make forward projections (earthcasts) of both fast and slow changes in the CZ. We are developing a cascade of models to use in earthcasting and learning how to extrapolate them across spatial and temporal scales (Duffy et al., 2014; Godderis and Brantley, 2014). One outcome of this will be models that can predict regolith characteristics as a function of geological and climatological history; because much groundwater flow is through regolith, this effort informs our hydrologic models. The trajectory of our work will eventually provide models that can predict changes in the fluxes of water, energy, gases, sediments, and solutes across timescales from 10^{-4} (water) to 10^{6} yr (regolith). For the sedimentary rocks underlying our CZO, we use these models to explore how the geological past and the Anthropocene present have impacted the structure of the regolith and, in turn, how this structure can affect fluxes today and in the future using scenarios of human behavior.

Acknowledgments

This research was conducted in Penn State's Stone Valley Forest, which is funded by the Penn State College of Agriculture Sciences, Department of Ecosystem Science and Management, and managed by the staff of the Forestlands Management Office. Financial Support was provided by National Science Foundation Grant EAR–0725019 (C. Duffy), EAR–1239285 (S. Brantley), and EAR–1331726 (S. Brantley) for the Susquehanna Shale Hills Critical Zone Observatory. Logistical support and/or data were provided by the NSF-supported Susquehanna Shale Hills Critical Zone Observatory.

References

Andrews, D. 2011. Coupling dissolved organic carbon and hydropedology in the Shale Hills Critical Zone Observatory. Ph.D. diss. Pennsylvania State Univ., University Park.

Andrews, D.M., H. Lin, Q. Zhu, L. Jin and S.L. Brantley. 2011. Hot spots and hot moments of dissolved organic carbon export and soil organic carbon storage in the Shale Hills catchment. Vadose Zone J. 10:943–954. doi:10.2136/vzj2010.0149

Baldwin, D. 2011. Catchment-scale soil water retention characteristics and delineation of hydropedological functional units in the Shale Hills catchment. M.S. thesis. Pennsylvania State Univ., University Park.

Baldwin, D., K.J. Naithani, and H. Lin. 2017. Combined soil-terrain stratification for characterizing catchment-scale soil moisture variation. Geoderma 285:260–269. doi:10.1016/j.geoderma.2016.09.031

Bao, C., L. Li, Y. Shi, and C.J. Duffy. 2017. Understanding watershed hydrogeochemistry: 1. Development of RT-Flux-PIHM. Water Resour. Res. 53:2328–2345. doi:10.1002/2016WR018934

Barr, A.G., A.D. Richardson, D.Y. Hollinger, D. Papale, M.A. Arain, T.A. Black, et al. 2013. Use of change-point detection for friction–velocity threshold evaluation in eddy-covariance studies. Agric. For. Meteorol. 171–172:31–45. doi:10.1016/j.agrformet.2012.11.023

Böhm, W. 1979. Methods of studying root systems. Springer, Berlin. doi:10.1007/978-3-642-67282-8

Brantley, S.L., H. Buss, M. Lebedeva, R.C. Fletcher, and L. Ma. 2011. Investigating the complex interface where bedrock transforms to regolith. Appl. Geochem. 26:S12–S15. doi:10.1016/j.apgeochem.2011.03.017

Brantley, S.L., R.A. DiBiase, T.A. Russo, Y. Shi, H. Lin, K.J. Davis, et al. 2016. Designing a suite of measurements to understand the critical zone. Earth Surf. Dyn. 4:211–235. doi:10.5194/esurf-4-211-2016

Brantley, S.L., M. Holleran, L. Jin, and E. Bazilevskaya. 2013. Probing deep weathering in the Shale Hills Critical Zone Observatory, Pennsylvania (USA): The hypothesis of nested chemical reaction fronts in the subsurface. Earth Surf. Processes Landforms 38:1280–1298. doi:10.1002/esp.3415

Brantley, S.L., M.I. Lebedeva, V.N. Balashov, K. Singha, P.L. Sullivan, and G. Stinchcomb. 2017a. Toward a conceptual model relating chemical reaction fronts to water flow paths in hills. Geomorphology 277:100–117. doi:10.1016/j.geomorph.2016.09.027

Brantley, S.L., W.H. McDowell, W.E. Dietrich, T.S. White, P. Kumar, S.P. Anderson, et al. 2017b. Designing a network of critical zone observatories to explore the living skin of the terrestrial Earth. Earth Surf. Dyn. 5:841–860. doi:10.5194/esurf-5-841-2017

Braun, D.D. 1989. Glacial and periglacial erosion of the Appalachians. Geomorphology 2:233–256. doi:10.1016/0169-555X(89)90014-7

Castellano, M.J., J.P. Schmidt, J.P. Kaye, C. Walker, C.B. Graham, H. Lin, and C.J. Dell. 2010. Hydrological and biogeochemical controls on the timing and magnitude of nitrous oxide flux across an agricultural landscape. Global Change Biol. 16:2711–2720. doi:10.1111/j.1365-2486.2009.02116.x

CASTNET. 2016. Clean Air Status and Trends Network Annual Dry Deposition: Penn State (PSU106) Station. [Data set.] USEPA, Washington, DC.

Chen, F. and J. Dudhia. 2001. Coupling an advanced land surface–hydrology model with the Penn State–NCAR MM5 modeling system: I. Model implementation and sensitivity. Mon. Weather Rev. 129:569–585. doi:10.1175/1520-0493(2001)129<0569:CAALSH>2.0.CO;2.

Chen, W., R.T. Koide, T.S. Adams, J.L. DeForest, L. Cheng, and D.M. Eissenstat. 2016. Root morphology and mycorrhizal symbioses together shape nutrient foraging strategies of temperate trees. Proc. Natl. Acad. Sci. 113:8741–8746. doi:10.1073/pnas.1601006113

Chen, W., R.T. Koide, and D.M. Eissenstat. 2018. Root morphology and mycorrhizal type strongly influence root production in nutrient hot spots of mixed forests. J. Ecol. 106:148–156. doi:10.1111/1365-2745.12800

Ciolkosz, E.J., W.J. Waltman, T.W. Simpson, and R.R. Dobos. 1989. Distribution and genesis of soils of the northeastern United States. Geomorphology 2:285–302. doi:10.1016/0169-555X(89)90016-0

Clark, G.M., and E.J. Ciolkosz. 1988. Periglacial geomorphology of the Appalachian Highlands and Interior Highlands south of the glacial border: A review. Geomorphology 1:191–220. doi:10.1016/0169-555X(88)90014-1

Clark, K.L., N. Skowronski, and J. Hom. 2010. Invasive insects impact forest carbon dynamics. Global Change Biol. 16:88–101. doi:10.1111/j.1365-2486.2009.01983.x

Cotter, E., and J.D. Inners. 1986. Silurian stratigraphy and sedimentology in the Huntingdon County area. In: W. Sevon, editor, 51st Annual Field Conference of Pennsylvania Geologists, Junita College, PA. Dep. of Environ. Resour., Bur. of Topogr. and Geol. Surv., Harrisburg. p. 27–39, 154–170.

Dahlgren, R.A. 1994. Soil acidification and nitrogen saturation from weathering of ammonium-bearing rock. Nature 368:838–841. doi:10.1038/368838a0

Dere, A.L., T.S. White, R.H. April, B. Reynolds, T.E. Miller, E.P. Knapp, et al. 2013. Climate dependence of feldspar weathering in shale soils along a latitudinal gradient. Geochim. Cosmochim. Acta 122:101–126. doi:10.1016/j.gca.2013.08.001

Duffy, C., Y. Shi, K. Davis, R. Slingerland, L. Li, P.L. Sullivan, et al. 2014. Designing a suite of models to explore critical zone function. Procedia Earth Planet. Sci. 10:7–15. doi:10.1016/j.proeps.2014.08.003

Ek, M.B., K.E. Mitchell, Y. Lin, E. Rogers, P. Grummann, V. Koren, et al. 2003. Implementation of Noah land surface model advances in the National Centers for Environmental Prediction operational mesoscale Eta model. J. Geophys. Res. 108:8851. doi:10.1029/2002JD003296

Field, J.P., D.D. Breshears, D.J. Law, J.C. Villegas, L. Lopez-Hoffman, P.D. Brooks, et al. 2015. Critical zone services: Expanding context, constraints, and currency beyond ecosystem services. Vadose Zone J. 14(1). doi:10.2136/vzj2014.10.0142

Gaines, K.P., F.C. Meinzer, C.J. Duffy, E.M. Thomas, and D.M. Eissenstat. 2016a. Rapid tree water transport and residence times in a Pennsylvania catchment. Ecohydrology 9:1554–1565. doi:10.1002/eco.1747

Gaines, K.P., J.W. Stanley, F.C. Meinzer, K.A. McCulloh, D.R. Woodruff, W. Chen, et al. 2016b. Reliance on shallow soil water in a mixed-hardwood forest in central Pennsylvania. Tree Physiol. 36:444–458. doi:10.1093/treephys/tpv113

Gerke, H.H., and M.Th. van Genuchten. 1993. A dual-porosity model for simulating the preferential movement of water and solutes in structured porous media. Water Resour. Res. 29:305–319.

Godderis, Y., and S.L. Brantley. 2014. Earthcasting the future critical zone. Elementa 1:19. doi:10.12952/journal.elementa.000019

Goulden, M.L., J.W. Munger, S.-M. Fan, B.C. Daube, and S.C. Wofsy. 1996. Measurements of carbon sequestration by long-term eddy covariance: Methods and a critical evaluation of accuracy. Global Change Biol. 2:169–182. doi:10.1111/j.1365-2486.1996.tb00070.x

Graham, C., and H. Lin. 2011. Controls and frequency of preferential flow occurrence: A 175-event analysis. Vadose Zone J. 10: 816–831. doi:10.2136/vzj2010.0119

Guo, L., J. Chen, and H. Lin. 2014. Subsurface lateral flow network on a hillslope revealed by time-lapse ground penetrating radar. Water Resour. Res. 50:9127–9147. doi:10.1002/2013WR014603

Guo, Q. 2010. Susquehanna Shale Hills Critical Zone Observatory: Leaf off survey. [Data set.] Open Topography. doi:10.5069/G9VM496T

Hadley, J.L., P.S. Kuzeja, M.J. Daley, N.G. Phillips, T. Mulcahy, and S. Singh. 2008. Water use and carbon exchange of red oak- and eastern hemlock-dominated forests in the northeastern USA: Implications for ecosystem-level effects of hemlock woolly adelgid. Tree Physiol. 28:615–627. doi:10.1093/treephys/28.4.615

Hasenmueller, E.A., X. Gu, J.N. Weitzman, T.S. Adams, G.E. Stinchcomb, D.M. Eissenstat, et al. 2017. Weathering of rock to regolith: The activity of deep roots in bedrock fracture. Geoderma 300:11–31. doi:10.1016/j.geoderma.2017.03.020

Herndon, E.M., and S.L. Brantley. 2011. Movement of manganese contamination through the critical zone. Appl. Geochem. 26:S40–S43. doi:10.1016/j.apgeochem.2011.03.024

Herndon, E.M., A.L. Dere, P.L. Sullivan, D. Norris, B. Reynolds and S.L. Brantley. 2015a. Landscape heterogeneity drives contrasting concentration–discharge relationships in shale headwater catchments. Hydrol. Earth Syst. Sci. 19:3333–3347. doi:10.5194/hess-19-3333-2015

Herndon, E., L. Jin, D.M. Andrews, D. Eissenstat, and S.L. Brantley. 2015b. Importance of vegetation for manganese cycling in temperate forested watersheds. Global Biogeochem. Cycles 29:160–174. doi:10.1002/2014GB004858

Herndon, E.M., L. Jin, and S.L. Brantley. 2011. Soils reveal widespread manganese enrichment from industrial inputs. Environ. Sci. Technol. 45:241–247. doi:10.1021/es102001w

Herndon, E.M., C.E. Martinez, and S.L. Brantley. 2014. Spectroscopic (XANES/XRF) characterization of contaminant manganese cycling in a temperate watershed. Biogeochemistry 121:505–517. doi:10.1007/s10533-014-0018-7

Herndon, E.M., G. Steinheofel, A.L.D. Dere, and P.L. Sullivan. 2018. Perennial flow through convergent hillslopes explains chemodynamic solute behavior in a shale headwater catchment. Chem. Geol. 493:413–425. doi:10.1016/j.chemgeo.2018.06.019

Iavorivska, L., E.W. Boyer, J.W. Grimm, M.P. Miller, D.R. DeWalle, K.J. Davis, and M.W. Kaye. 2017. Variability of dissolved organic carbon in precipitation during storms at the Shale Hills Critical Zone Observatory. Hydrol. Processes 31:2935–2950. doi:10.1002/hyp.11235

Isaaks, E.H., and R.M. Srivastava. 1989. An introduction to applied geostatistics. Oxford Univ. Press, New York.

Jin, L., D.M. Andrews, G.H. Holmes, H. Lin and S.L. Brantley. 2011a. Opening the "black box": Water chemistry reveals hydrological controls on weathering in the Susquehanna Shale Hills Critical Zone Observatory. Vadose Zone J. 10:928–942. doi:10.2136/vzj2010.0133

Jin, L., N. Ogrinc, T. Yesavage., E.A. Hasenmueller, L. Ma, P.L. Sullivan, et al. 2014. The CO_2 consumption potential during gray shale weathering: Insights from the evolution of carbon isotopes in the Susquehanna Shale Hills Critical Zone Observatory. Geochim. Cosmochim. Acta 142:260–280. doi:10.1016/j.gca.2014.07.006

Jin, L., R. Ravella, B. Ketchum, P.R. Bierman, P. Heaney, T.S. White, and S.L. Brantley. 2010. Mineral weathering and elemental transport during hillslope evolution at the Susquehanna/Shale Hills Critical Zone Observatory. Geochim. Cosmochim. Acta 74:3669–3691. doi:10.1016/j.gca.2010.03.036

Jin, L., G. Rother, D. Cole, D. Mildner, C.J. Duffy, and S.L. Brantley. 2011b. Characterization of deep weathering and nanoporosity development in shale: A neutron study. Am. Mineral. 96:498–512. doi:10.2138/am.2011.3598

Johnson, D.W. 1992. Nitrogen retention in forest soils. J. Environ. Qual. 21:1–12. doi:10.2134/jeq1992.00472425002100010001x

Kalnay, E., M. Kanamitsu, R. Kistler, W. Collins, D. Deaven, L. Gandin, et al. 1996. The NCEP/NCAR 40-Year Reanalysis Project. Bull. Am. Meteorol. Soc. 77:437–471. doi:10.1175/1520-0477(1996)077<0437:TNYRP>2.0.CO;2

Kljun, N., P. Calanca, M.W. Rotach, and H.P. Schmid. 2015. A simple two-dimensional parameterisation for Flux Footprint Prediction (FFP). Geosci. Model Dev. 8:3695–3713. doi:10.5194/gmd-8-3695-2015

Kraepiel, A.M., A.L. Dere, E.M. Herndon, and S.L. Brantley. 2015. Natural and anthropogenic processes contributing to metal enrichment in surface soils of central Pennsylvania. Biogeochemistry 123:265–283. doi:10.1007/s10533-015-0068-5

Kuntz, B., S. Rubin, B. Berkowitz, and K. Singha. 2011. Quantifying solute transport behavior at the Shale Hills Critical Zone Observatory. Vadose Zone J. 10:843–857. doi:10.2136/vzj2010.0130

Li, L., C. Bao, P.L. Sullivan, S. Brantley, Y. Shi, and C. Duffy. 2017a. Understanding watershed hydrogeochemistry: 2. Synchronized hydrological and geochemical processes drive stream chemostatic behavior. Water Resour. Res. 53:2346–2367. doi:10.1002/2016WR018935

Li, L., R.A. DiBiase, J. Del Vecchio, V. Marcon, B. Hoagland, D. Xiao, et al. 2018. Investigating the effect of lithology and agriculture at the Susquehanna Shale Hills Critical Zone Observatory (SSHCZO): The Garner Run and Cole Farm subcatchments. Vadose Zone J. 17:180063. doi:10.2136/vzj2018.03.0063

Li, L., K. Maher, A. Navarre-Sitchler, J. Druhan, C. Meile, C. Lawrence, et al. 2017b. Expanding the role of reactive transport models in critical zone processes. Earth-Sci. Rev. 165:280–301. doi:10.1016/j.earscirev.2016.09.001

Lin, H. 2006. Temporal stability of soil moisture spatial pattern and subsurface flow pathways in the Shale Hills catchment. Vadose Zone J. 5:317–340. doi:10.2136/vzj2005.0058

Lin, H. 2014. Shale Hills: Hydropedologic properties, soil temperature (2007–2014). [Data set.] Susquehanna Shale Hills Critical Zone Observatory, PA. http://criticalzone.org/shale-hills/data/dataset/2587/ (accessed 16 Apr. 2018).

Lin, H.S., W. Kogelmann, C. Walker, and M.A. Bruns. 2006. Soil moisture patterns in a forested catchment: A hydropedological perspective. Geoderma 131:345–368. https://doi.org/10.1016/j.geoderma.2005.03.013

Lin, H., and X. Zhou. 2008. Evidence of subsurface preferential flow using soil hydrologic monitoring in the Shale Hills catchment. Eur. J. Soil Sci. 59:34–49. doi:10.1111/j.1365-2389.2007.00988.x

Liu, H., and H. Lin. 2015. Frequency and control of subsurface preferential flow: From pedon to catchment scales. Soil Sci. Soc. Am. J. 79:362–377. doi:10.2136/sssaj2014.08.0330

Lynch, J. 1976. Effects of antecedent moisture on storage hydrographs. Ph.D. diss. Pennsylvania State Univ., University Park.

Ma, L., F. Chabaux, E. Pelt, E. Blaes, L. Jin, and S. Brantley. 2010. Regolith production rates calculated with uranium-series isotopes at the Susquehanna/Shale Hills Critical Zone Observatory. Earth Planet. Sci. Lett. 297:211–225. doi:10.1016/j.epsl.2010.06.022

Ma, L., F. Chabaux, N. West, E. Kirby, L. Jin and S.L. Brantley. 2013. Regolith production and transport in the Susquehanna Shale Hills Critical Zone Observatory: 1. Insights from U-series isotopes. J. Geophys. Res. Earth

Surf. 118:722–740. doi:10.1002/jgrf.20037

Ma, L., J. Konter, E. Herndon, L. Jin, G. Steinhoefel, D. Sanchez, and S. Brantley. 2014. Quantifying an early signature of the industrial revolution from lead concentrations and isotopes in soils of Pennsylvania, USA. Anthropocene 7:16-29. doi:10.1016/j.ancene.2014.12.003

Meek, K., L. Derry, J. Sparks, and L. Cathles. 2016. $^{87}Sr/^{86}Sr$, Ca/Sr, and Ge/Si ratios as tracers of solute sources an biogeochemical cycling at a temperate forested shale catchment, central Pennsylvania, USA. Chem. Geol. 445:84–102. doi:10.1016/j.chemgeo.2016.04.026

Meinzer, F., D.M. Eissenstat, and H. Lin. 2013. Above- and belowground controls on water use by trees of different wood types in an eastern United States deciduous forest. Tree Physiol. 33:345–356. doi:10.1093/treephys/tpt012

Meyer, S.C., D.A. Textoris, and J.M. Dennison. 1992. Lithofacies of the Silurian Keefer Sandstone, east-central Appalachian basin, USA. Sediment. Geol. 76:187–206. doi:10.1016/0037-0738(92)90083-4

National Atmospheric Deposition Program. 2016. Nitrogen from the atmosphere. ISWS Misc. Publ. 207. NADP, Illinois State Water Surv., Champaign.

NOAA. 2007. U.S. divisional and station climatic data and normals. [Database.] Natl. Clim. Data Ctr., Asheville, NC.

Noireaux, J., J. Gaillardet, P. Sullivan, and S.L. Brantley. 2014. Boron isotope fractionation in soils at the Shale Hills CZO. Procedia Earth Planet. Sci. 10:218–222. doi:10.1016/j.proeps.2014.08.024

Nutter, W.L. 1964. Determination of the head–discharge relationship for a sharp-crested compound weir and a sharp-crested parabolic weir. M.S. thesis. Pennsylvania State Univ., University Park, PA.

Nyquist, J.E., L. Toran, L. Pitman, L. Guo, and H. Lin. 2018. Testing the fill-and-spill model of subsurface lateral flow using ground-penetrating radar and dye tracing. Vadose Zone J. 17:170142. doi:10.2136/vzj2017.07.0142

Odeh, I., A. McBratney, and D. Chittleborough. 1995. Further results on prediction of soil properties from terrain attributes: Heterotopic cokriging and regression-kriging. Geoderma 67:215–226. doi:10.1016/0016-7061(95)00007-B

Qu, Y. and C.J. Duffy. 2007. A semi-discrete finite volume formulation for multiprocess watershed simulation. Water Resour. Res. 43:W08419. doi:10.1029/2006WR005752

Rempe, D.M., and W.E. Dietrich. 2014. A bottom-up control on fresh-bedrock topography under landscapes. Proc. Natl. Acad. Sci. 111:6576–6581. doi:10.1073/pnas.1404763111

Rice, K.C., T.M. Scanlon, J.A. Lynch, and B.J. Cosby. 2014. Decreased atmospheric sulfur deposition across the southeastern U.S.: When will watersheds release stored sulfate? Environ. Sci. Technol. 48:10071–10078. doi:10.1021/es501579s

Shi, Y., K.J. Davis, C.J. Duffy, and X. Yu. 2013. Development of a coupled land surface hydrologic model and evaluation at a critical zone observatory. J. Hydrometeorol. 14:1401–1420. doi:10.1175/JHM-D-12-0145.1

Shi, Y., K.J. Davis, F. Zhang, C.J. Duffy, and X. Yu. 2015. Parameter estimation of a physically-based land surface hydrologic model using an ensemble Kalman filter: A multivariate real-data experiment. Adv. Water Resour. 83:421–427. doi:10.1016/j.advwatres.2015.06.009

Shi, Y., D.M. Eissenstat, Y. He, and K.J. Davis. 2018. Using a spatially-distributed hydrologic biogeochemistry model with a nitrogen transport module to study the spatial variation of carbon processes in a critical zone observatory. Ecol. Modell. 380:8–21. doi:10.1016/j.ecolmodel.2018.04.007

Slim, M., J.T. Perron, S.J. Martel, and K. Singha. 2015. Topographic stress and rock fracture: A two-dimensional numerical model for arbitrary topography and preliminary comparison with borehole observations. Earth Surf. Processes Landforms 40:512–529. doi:10.1002/esp.3646

Smith, L.A., D.M. Eissenstat, and M.W. Kaye. 2017. Variability in aboveground carbon driven by slope aspect and curvature in an eastern deciduous forest, USA. Can. J. For. Res. 47:149–158. doi:10.1139/cjfr-2016-0147

Sposito, G., editor. 1998. Scale dependence and scale invariance. Cambridge Univ. Press, Cambridge, UK. doi:10.1017/CBO9780511551864

Sullivan, P.L., S. Hynek, X. Gu, K. Singha, T.S. White, N. West, et al. 2016a. Oxidative dissolution under the channel leads geomorphological evolution at the Shale Hills catchment. Am. J. Sci. 316:981–1026. doi:10.2475/10.2016.02

Sullivan, P.L., L. Ma, N. West, L. Jin, D.L. Karwan, J. Noireaux, et al. 2016b. CZ-tope at the Susquehanna Shale Hills CZO: Synthesizing multiple isotope proxies to elucidate critical zone processes across timescales in a temperate forested landscape. Chem. Geol. 445:103–119. doi:10.1016/j.chemgeo.2016.05.012

Swain, F.M. 1966. Coal science. Am. Chem. Soc., Washington, DC.

Thomas, E., H. Lin, C. Duffy, P. Sullivan, G.H. Holmes, S.L. Brantley, and L. Jin. 2013. Spatiotemporal patterns of water stable isotope compositions at the Shale Hills Critical Zone Observatory: Linkages to subsurface hydrologic processes. Vadose Zone J. 12(4). doi:10.2136/vzj2013.01.0029

Thornton, P.E., B.E. Law, H.L. Gholz, K.L. Clark, E. Falge, D.S. Ellsworth, et al. 2002. Modeling and measuring the effects of disturbance history and climate on carbon and water budgets in evergreen needleleaf forests. Agric. For. Meteorol. 113:185–222. doi:10.1016/S0168-1923(02)00108-9

Vickers, D. and L. Mahrt. 1997. Quality control and flux sampling problems for tower and aircraft data. J. Atmos. Oceanic Technol. 14:512–526. doi:10.1175/1520-0426(1997)014<0512:QCAFSP>2.0.CO;2

Weitzman, J.N., and J.P. Kaye. 2016. Variability in soil nitrogen retention across forest, urban, and agricultural land uses. Ecosystems 19:1345–1361. doi:10.1007/s10021-016-0007-x

Weitzman, J.N., and J.P. Kaye. 2018. Nitrogen budget and topographic controls on nitrous oxide in a shale-based watershed. J. Geophys. Res. Biogeosci. 123:1888–1908. doi:10.1029/2017JG004344

Wen, H., and L. Li. 2018. An upscaled rate law for mineral dissolution in heterogeneous media: The role of time and length scales. Geochem. Cosmochem. Acta 235:1–20. doi:10.1016/j.gca.2018.04.024

West, N. 2014. Topographic fingerprints of hillslope erosion in the Central Appalachians revealed by meteoric beryllium-10. Ph.D. diss. Pennsylvania State Univ., University Park.

West, N., E. Kirby, P. Bierman, and B. Clarke. 2014. Aspect-dependent variations in regolith creep revealed by meteoric ^{10}Be. Geology 42:507–510. doi:10.1130/G35357.1

West, N., E. Kirby, P. Bierman, R. Slingerland, L. Ma and S.L. Brantley. 2013. Regolith production and transport in the Susquehanna Shale Hills Critical Zone Observatory: 2. Insights from meteoric ^{10}Be. J. Geophys. Res. Earth Surf. 118:1877–1896. doi:10.1002/jgrf.20121

Yesavage, T., M. Fantle, J. Vervoort, R. Mathur, L. Jin, L. Liermann, and S.L. Brantley. 2012. Fe cycling in the Shale Hills Critical Zone Observatory, Pennsylvania: An analysis of biogeochemical weathering and Fe isotope fractionation. Geochim. Cosmochim. Acta 99:18–38. doi:10.1016/j.gca.2012.09.029

Yi, C., K.J. Davis, P.S. Bakwin, B.W. Berger, and L.C. Marr. 2000. Influence of advection on measurements of the net ecosystem–atmosphere exchange of CO_2 from a very tall tower. J. Geophys. Res. 105(D8):9991–9999. doi:10.1029/2000JD900080

Yu, H., P. Yang, and H. Lin. 2015. Spatiotemporal patterns of soil matric potential in the Shale Hills Critical Zone Observatory. Vadose Zone J. 14(7). doi:10.2136/vzj2014.11.0167

Zhang, J., H. Lin, and J. Doolittle. 2014. Soil layering and preferential flow impacts on seasonal changes of GPR signals in two contrasting soils. Geoderma 213:560–569. doi:10.1016/j.geoderma.2013.08.035

Zreda, M., W.J. Shuttleworth, X. Xeng, C. Zweck, D. Desilets, T.E. Franz, and R. Rosolem. 2012. COSMOS: The COsmic-ray Soil Moisture Observing System. Hydrol. Earth Syst. Sci. 16:4079–4099. doi:10.5194/hess-16-4079-2012